2004-01

Laminar Cortical Dynamics of 3D Surface Perception: Stratification, transparency, and Neon Color Spreading

Laminar cortical dynamics of 3D surface perception: Stratification, transparency, and neon color spreading

Stephen Grossberg and Arash Yazdanbakhsh

January, 2004

Technical Report CAS/CNS-2004-002

Boston University Center for Adaptive Systems
and
Department of Cognitive and Neural Systems
677 Beacon Street
Boston, MA 02215

Laminar Cortical Dynamics of 3D Surface Perception: Stratification, Transparency, and Neon Color Spreading

Stephen Grossberg and Arash Yazdanbakhsh[1]

Department of Cognitive and Neural Systems
and
Center for Adaptive Systems
Boston University
677 Beacon Street, Boston, MA 02215
Phone: 617-353-7858
Fax: 617-353-7755

Technical Report CAS/CNS TR-2004-002
Submitted: January 27, 2004

All correspondence should be addressed to
Professor Stephen Grossberg
Department of Cognitive and Neural Systems
Boston University
677 Beacon Street
Boston, MA 02215
Phone: 617-353-7858
Fax: 617-353-7755
Email:steve@bu.edu

[1] Authorship in alphabetical order. SG was supported in part by the Air Force Office of Scientific Research (AFOSR F49620-01-1-0397) and the office of Naval Research (ONR N00014-01-1-0624). AY was Supported in part by the Office of Naval Research (ONR N00014-01-1-0624)

Abstract

How does the laminar organization of cortical circuitry in areas V1 and V2 give rise to 3D percepts of stratification, transparency, and neon color spreading in response to 2D pictures and 3D scenes? Psychophysical experiments have shown that such 3D percepts are sensitive to whether contiguous image regions have the same relative contrast polarity (dark-light or light-dark), yet long-range perceptual grouping is known to pool over opposite contrast polarities. The ocularity of contiguous regions is also critical for neon color spreading: Having different ocularity despite the contrast relationship that favors neon spreading blocks the spread. In addition, half visible points in a stereogram can induce near-depth transparency if the contrast relationship favors transparency in the half visible areas. It thus seems critical to have the whole contrast relationship in a monocular configuration, since splitting it between two stereogram images cancels the effect. What adaptive functions of perceptual grouping enable it to both preserve sensitivity to monocular contrast and also to pool over opposite contrasts? Aspects of cortical development, grouping, attention, perceptual learning, stereopsis and 3D planar surface perception have previously been analyzed using a 3D LAMINART model of cortical areas V1, V2, and V4. The present work consistently extends this model to show how like-polarity competition between V1 simple cells in layer 4 may be combined with other LAMINART grouping mechanisms, such as cooperative pooling of opposite polarities at layer 2/3 complex cells. The model also explains how the Metelli Rules can lead to transparent percepts, how bistable transparency percepts can arise in which either surface can be perceived as transparent, and how such a transparency reversal can be facilitated by an attention shift. The like-polarity inhibition prediction is consistent with lateral masking experiments in which two flanking Gabor patches with the same contrast polarity as the target increase the target detection threshold when they approach the target. It is also consistent with LAMINART simulations of cortical development. Other model explanations and testable predictions will also be presented.

Key Words: Surface Perception, Perceptual Grouping, 3D Vision, Visual Cortex, Figure-Ground Separation, Transparency, Neon Color Spreading, LAMINART, FACADE, Contrast Polarity.

1. Depthful grouping of 2D cues

Our visual systems construct 3D mental representations from pairs of 2D images on our two retinas. Binocular disparity information is a major cue in this reconstruction process. Depthful percepts can also be derived from a single monocularly viewed 2D image. Transparency (Figure 1) and neon color spreading (Figure 2) percepts illustrate this competence. Yet even these percepts can be strongly influenced by how 2D information is combined from both eyes (Anderson, 1997; Nakayama 1996). These percepts can also be generated or eliminated by changing the contrast relationship in a 2D picture without changing the geometrical layout of its edges (Anderson, 1997; Beck, 1984, Nakayama, 1996). These variations provide important clues to how the brain carries out normal 3D vision.

Sections 2 and 3 summarize how different contrast relationships within fixed geometrical combinations can determine the presence or absence of transparency and neon color phenomena in response to monocular and binocular presentations. These properties are used to refine a 3D LAMINART model of how cortical areas V1, V2, and V4 carry out 3D perceptual grouping and surface filling-in (Grossberg, 1999, 2003; Grossberg and Howe, 2003; Grossberg and Raizada, 2000; Grossberg and Seitz 2003; Grossberg and Swaminathan (2003); Grossberg and Williamson, 2001; Raizada and Grossberg, 2003). This refinement shows how the 3D LAMINART model can explain a wider range of 3D stratification, transparency, and neon color spreading, in addition to all the other data previously demonstrated to be within its explanatory and predictive range. The refinement claims that inhibitory interneurons within layer 4 of V1 prefer to contact cells that are sensitive to the same contrast polarity. This property is consistent with earlier modeling studies of V1 development (Grossberg and Williamson, 2001), but its perceptual implementations were not clear until now. These results have been briefly reported in Grosssberg and Yazdanbakhsh (2003a, 2003b).

2. Contrast relationships that induce transparency

The images in Figure 1 all have the same edge geometry (Figure 1d); however, we perceive them differently. In Figure 1a, the bottom square is perceived as a transparent layer over the top square. The opposite percept, with the bottom square being over the top one, does not occur. In Figure 1b, either square can be seen as a transparent surface over the other one. Figure 1c does not induce a percept of transparency. In addition, the dominant perceptual grouping looks like a bright small square in the middle that is surrounded by two dark L-shaped figures.

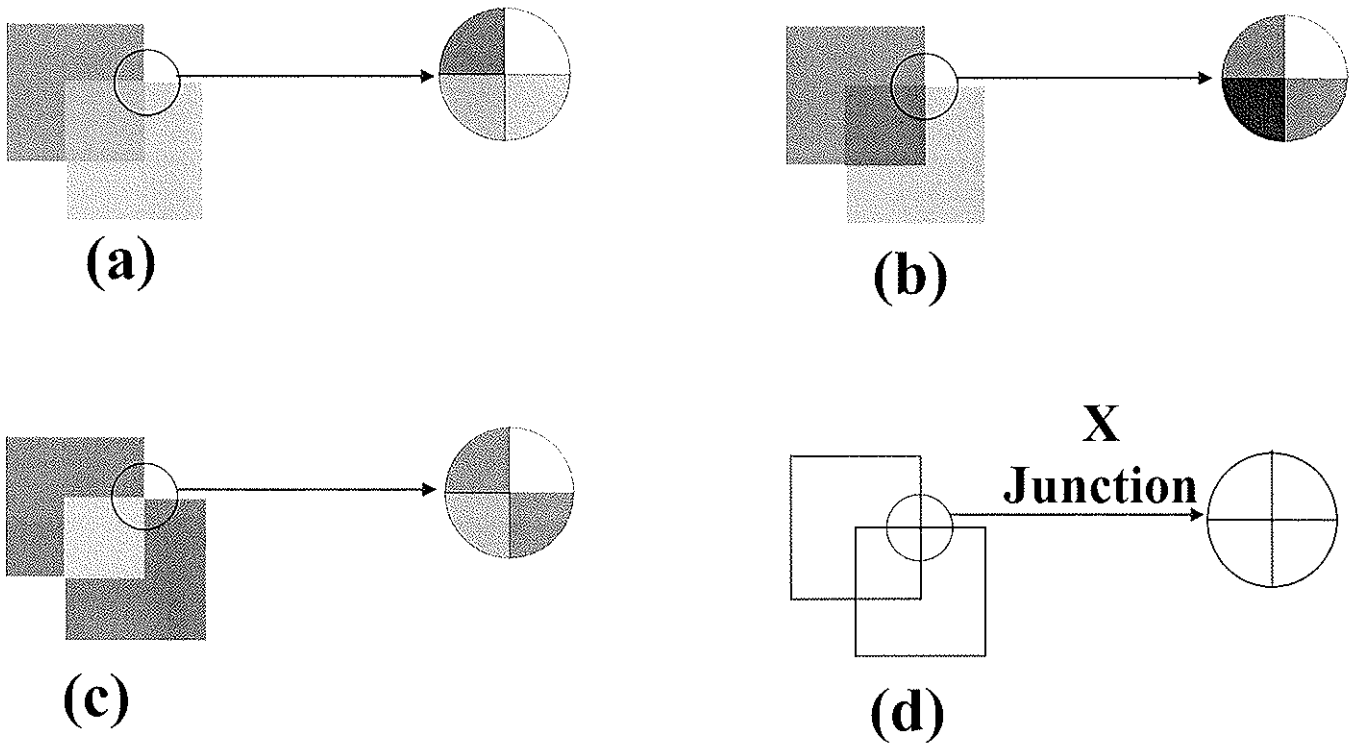

Figure 1. The correspondence between polarity alignment and the presence or absence of transparency: Each panel shows the specific contrast relationship that favors or does not favor transparency. (a) Single polarity reversal favors unique transparency. (b) No polarity reversal favors bistable transparency. (c) Double polarity reversal does not support transparency. (d) All of these images have the same geometry of edges.

These displays show that the relative contrasts at aligned edges of contiguous regions influence whether a transparency percept is perceived. The same contrast polarity at aligned edges of contiguous regions facilitates transparency, whereas opposite contrast polarities prevent transparency. Such a sensitivity to contrast polarity, points to an influence from an early stage of cortical processing, notably in V1. We are therefore led to ask: How does polarity-sensitive V1 processing alter the 3D perceptual groupings that occur in V2, and thus the visible 3D surface percepts that occur in V4?

Many researchers have noted the correspondence between contrast relations and the presence or absence of transparency (Adelson, 2000; Anderson, 1997; Beck, 1984; Metelli, 1974; Watanabe and Cavanaugh, 1992, 1993). If contrast polarity (dark-light versus light dark) is preserved along one branch of an X-junction, then unique transparency is seen (Figure 1a). Moreover, the X-junction branch along which polarity is preserved is part of a surface that is partially occluded by the transparent layer that is attached to the polarity-reversing edge. Preserving the contrast polarity along both branches, results in bistable transparency (Figure 1b). If polarity-reversal takes place along both branches, then the perceptual stratification fundamentally changes (Figure 1c): Depth stratification in the sense of one square over the other one disappears, and the middle small square seems more distinct.

3. Contrast relationships that induce neon color spreading

The different panels of Figure 2 have the same edge geometry but their different contrast relationships induce different percepts. In the neon color spreading case (Figure 2a), the contrast polarity along the T-junctions is preserved. In the non-neon case (Figure 2b), the polarity along the T-junctions reverses and no neon spreads.

The influence of like-polarity contrast relations both in transparency and neon color spreading focuses our attention upon early stages of V1 cortical processing. We claim that this like-polarity contrast sensitivity occurs in layer 4 of V1. The next section summarizes experimental evidence for this hypothesis.

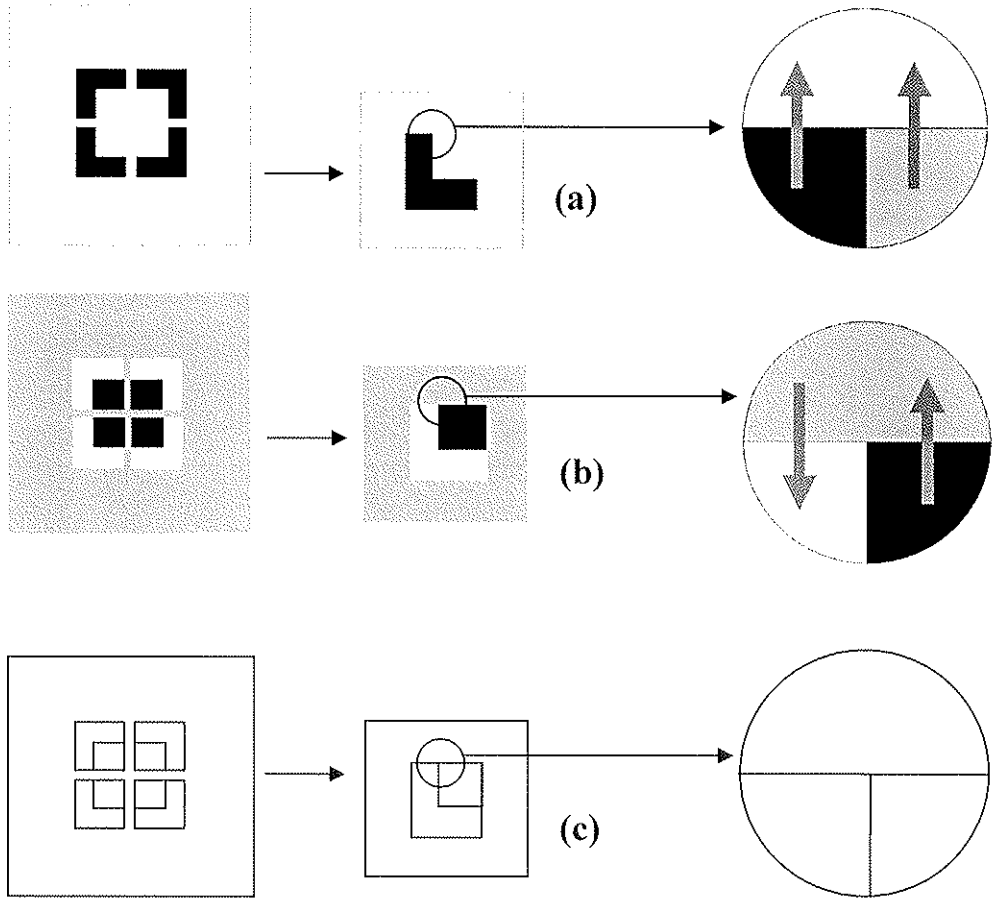

Figure 2. (a) Like-polarity contrasts favor neon color spreading: the T-junction is polarity preserving. (b) Opposite contrast polarities block neon color spreading: the T-junction is polarity reversing. (c) In both (a) and (b), the edge geometry, including all T-junctions, is the same.

4. Ocularity of contrast relations

Tacheichi, Shimojo and Watanabe (1993) showed that the contrast constraints that determine neon color spreading are monocularly computed (Figures 3 and 4). Fusing the stereogram in Figure 3 results in a percept of neon color spreading bounded by an illusory square. However,

fusing the stereogram in Figure 4 does not result in the neon color spreading. The illusory sides of the square exist without being filled with spreading gray color.

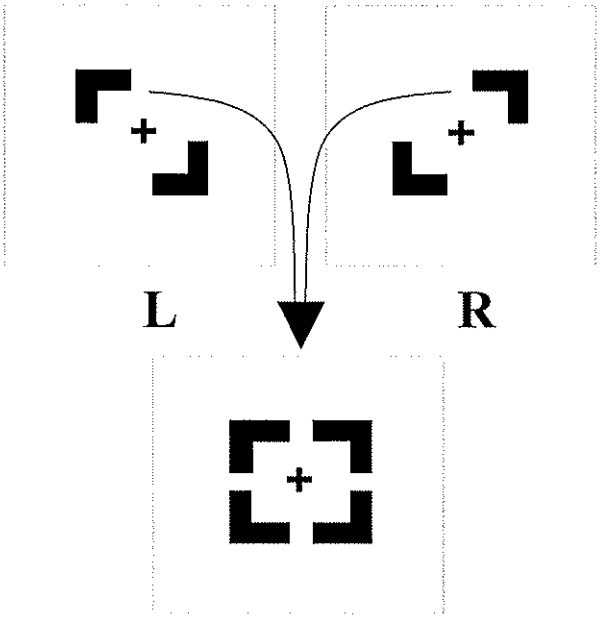

Figure 3. Splitting the inducers from Figure 2a across two eyes, while preserving the contrast relations within each eye, elicits neon color spreading. The illusory square bridges different ocularities.

This result shows that the contrast polarity constraint is *monocular*. In the other word, the contrast relation that favors neon spreading needs to be present completely in one eye in order to give rise to the neon effect. Previous 3D LAMINART modeling helps us to localize this constraint to layer 4 of cortical area V1, as indicated below.

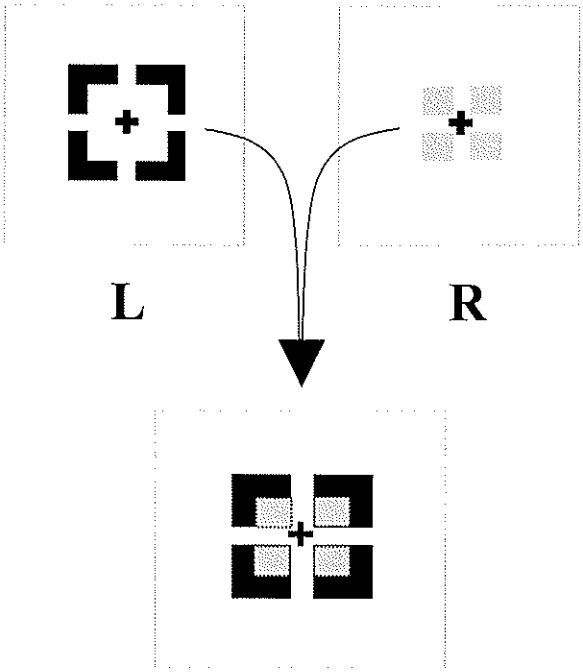

Figure 4. When the contrasts of Figure 2a are split between the two images of the stereogram, then fusion of the stereogram does not yield neon color spreading.

5. Locating the monocular contrast constraint in a V1 laminar circuit

In the 3D LAMINART model of Grossberg and Howe (2003), binocular fusion occurs in layer 3B of V1 (Figure 5). This means that, at this laminar stage, there are cells which have already lost ocularity and are influenced by both eyes. Noting the monocularity of the contrast polarity constraint, we propose that the polarity-specific monocular process occurs before layer 3B of V1, where it can discriminate between the split contrast and the non-split contrast constraints in Tacheichi et al. (1992).

Just knowing that the contrast constraint is monocular is not enough to localize the laminar cortical circuit responsible for it. More details are needed to make this constraint ready for rigorous implementation in the model. The next sections show that this polarity-specific monocular process is *monocular like-polarity competition.* This conclusion is derived by combining the perceptual constraints derived from the data summarized above with theoretical constraints that have been derived from earlier modeling efforts. These combined constraints lead to an unambiguous computational hypothesis.

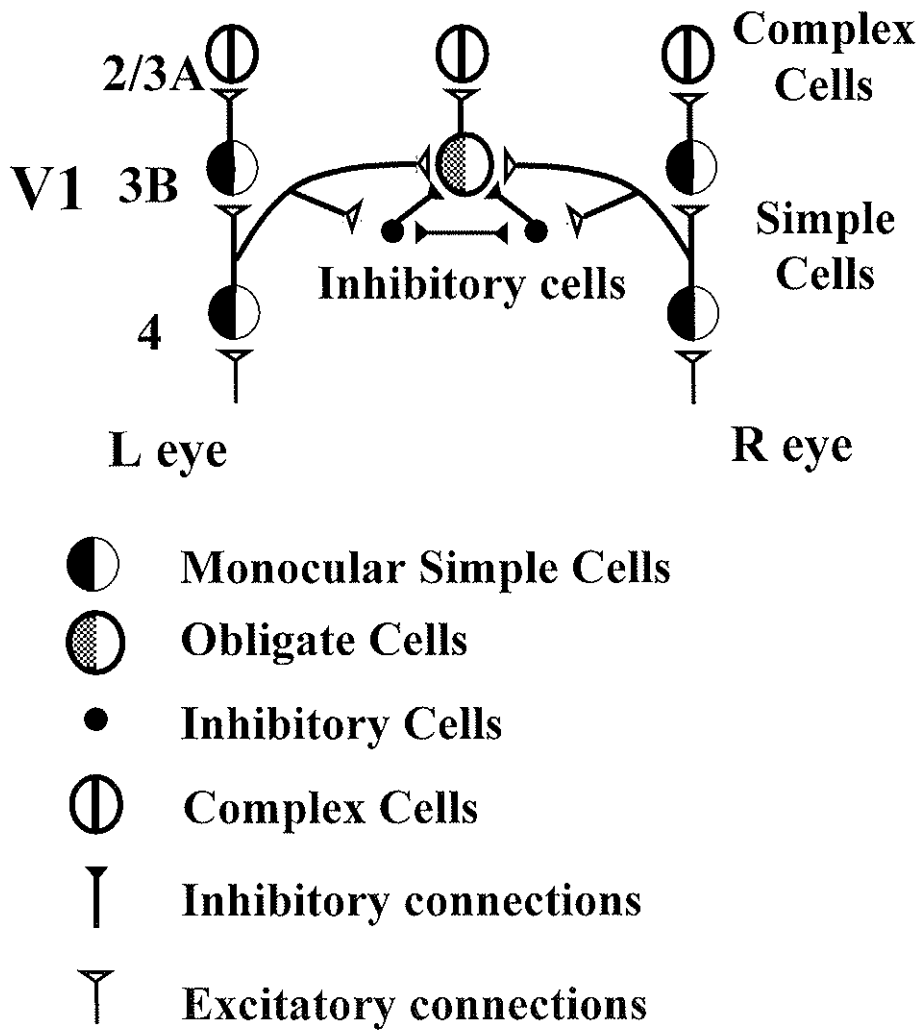

Figure 5. In the LAMINART model of Grossberg and Howe (2003), binocular fusion begins in layer 3B of V1. This fact suggests that the monocular contrast process occurs within layers before layer 3B of V1, notably the main input layer 4 of V1 (see Figure 7).

6. Contrast-polarity sensitivity versus contrast-polarity pooling

Another constraint on contrast polarity further localizes the monocular contrast constraint, but seems at the outset to be at odds with it. Figure 6 illustrates that perceptual boundaries can form around objects in front of textured backgrounds. To achieve this, the boundary grouping process pools signals from opposite contrast polarities at each position (Grossberg, 1994; Grossberg and Mingolla, 1985). In other words boundary grouping is *contrast-polarity invariant*.

How does the brain reconcile the coexistence of contrast-polarity sensitivity with contrast-polarity pooling for boundary formation? The 3D LAMINART model proposes that such pooling occurs in layer 2/3A of V1 after like-polarity binocular fusion occurs in layer 3B (Figure 5). Both of these constraints thus suggest that the monocular contrast constraint occurs early in V1. As noted above, we propose that it is realized by monocular like-polarity

competition in layer 4 of V1. How this hypothesis explains our targeted data can only be understood by analyzing its contextual effects within the entire 3D LAMINART circuit.

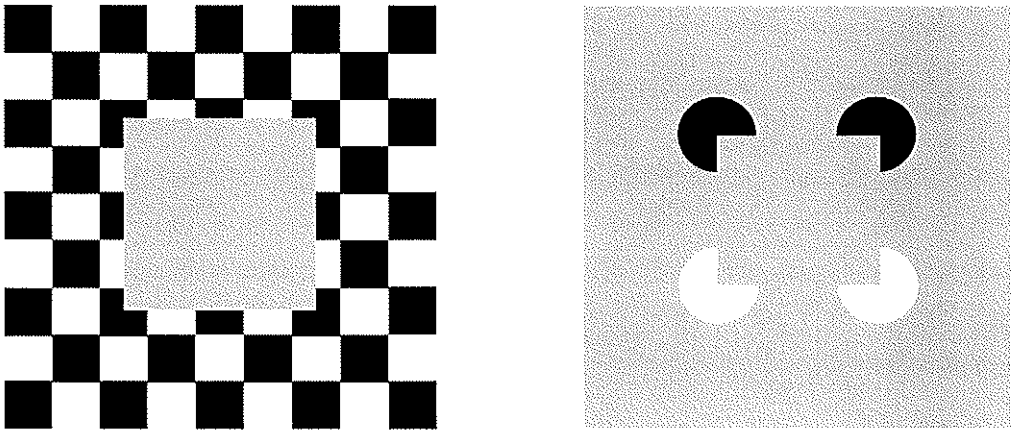

(a) (b)

Figure 6. (a) Boundary formation is contrast invariant: The polarity of contrasts along the square boundary reverses. However, these opposite contrasts are pooled by the brain to form the object boundary. (b) Long-range grouping to form the Kanizsa square pools over opposite contrast polarities.

7. 3D LAMINART circuit

Figure 7 summarizes how monocular polarity-specific competition is realized within the 3D LAMINART model. Earlier applications of the LAMINART model to explain data about 2D development, learning, grouping, and attention made heavy use of modulatory on-center off-surround circuit from layer 6 to 4 of V1; e.g. Grossberg (1999a); Grossberg, Mingolla, and Ross (1997); Grossberg and Raizada (2000). The 3D LAMINART model of Grossberg and Howe (2003) and Grossberg and Swaminathan (2003) were used to simulate data for which this circuit was not important, although both models showed how it could be implemented within the 3D model. Here we again make major use of this circuit and assume that it is the mechanism which underlies the monocular polarity constraint; see the V1 circuit surrounded by the dashed line in Figure 7. Like-polarity binocular fusion occurs at binocular simple cells in layer 3B of V1. Pooling of opposite contrast polarities occurs at complex cells in V1. Monocular and binocular signals are pooled at layer 4 of V2. A disparity filter also occurs in V2 to help solve the correspondence problem. Long-range contrast-invariant boundary completion, as in the Kanizsa square percept of Figure 6b, occurs in layer 2/3 of V2; see the V2 circuit surrounded by the dashed line in Figure 7. Grossberg and Howe (2003) summarize additional experimental support and theoretical explanations of the model.

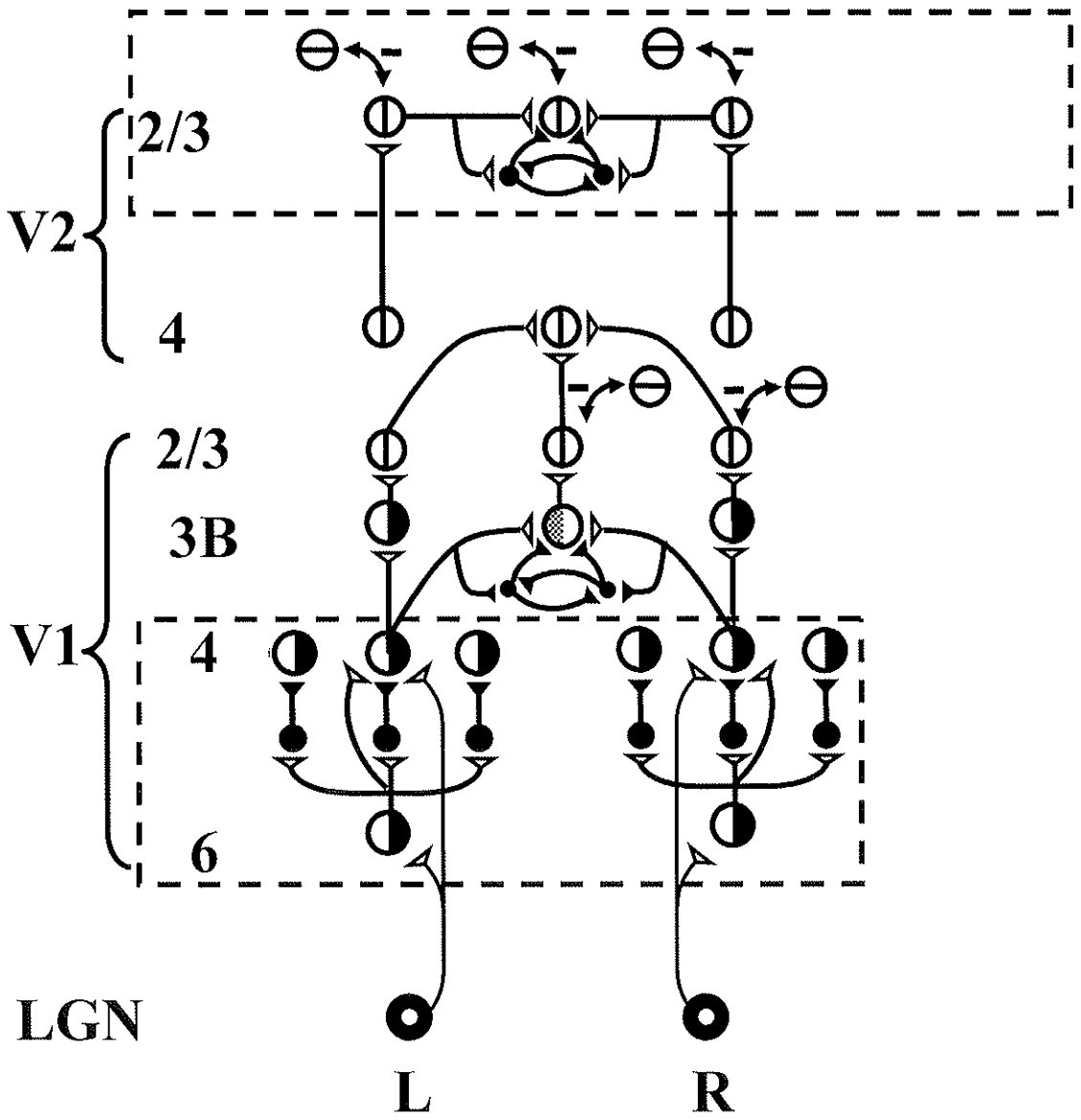

Figure 7. 3D LAMINART model: Before layer 3B of V1, the cells and their connections are eye specific. Like-polarity spatial competition in layer 4 implements the monocular contrast process. Long-range boundary grouping in layer 2/3 of V2 is both binocular and contrast invariant, because opposite eye streams have already been pooled in layer 3B of V1 and layer 4 of V2, and opposite contrasts have already been pooled in layer 2/3 of V1. These laminar circuits clarify how both contrast-polarity sensitive and contrast-polarity pooling processes can coexist together. In the upper dashed box of the figure, a set of vertically-oriented bipole cells are shown, each of them belongs to a group of colinear vertically-oriented bipole grouping cells.

8. Contrast influences both boundary and surface processing

Because contrasts are pooled to form long-range boundary groupings (Figure 7), such groupings do not generate a visible percept within the boundary grouping system, or BCS (see Figure 6b). A key hypothesis of FACADE theory is that visibility is a property of surface filling-in system, or FCS (Grossberg, 1994; Grossberg and Mingolla, 1985b).

Interactions between the BCS and FCS are proposed to lead to the visible 3D surface percepts that we explain herein. An early stage in this interaction uses the binocular boundaries in layer 2/3A of V2 (Figure 7) to selectively capture the monocular surface signals that will be visible at different depths (Figure 8). This surface capture process leads to a final percept of surfaces seen at different depths. Detailed explanations of how FACADE theory realizes 3D surface capture are found in several places; e.g., Grossberg (1994, 1997, 2003), Kelly and Grossberg (2000). Here we review just those properties that we need to explain the targeted data.

One such property is that the illuminant is discounted before the stage of depthful surface capture. This discounting process suppresses lightness and color signals within the interiors of regions with homogenous achromatic or chromatic contrast (Figure 9a). Surface lightness or color throughout these regions is recovered using boundary-gated filling-in of the lightness and color signals that survive the discounting process near positions of rapid contrast change. If the boundary corresponding to a surface border forms a closed contour, then it can contain the filling-in process (Figure 9b). If the boundary has large gaps, then the surface qualia can dissipate by spreading through the gaps (Figure 9c). Earlier studies of transparency, neon color spreading, and figure-ground separation proposed how cooperative-competitive interactions that select a winning boundary can sometimes create boundary gaps that use the dissipation property in Figure 9 to trigger the separation of surfaces in depth; e.g. Grossberg (1994, 1997, 1999a), Grossberg and Mingolla (1985a), Kelly and Grossberg (2000). Here we combine these FACADE mechanisms with the 3D LAMINART mechanisms in Figure 7 to explain and simulate the targeted data.

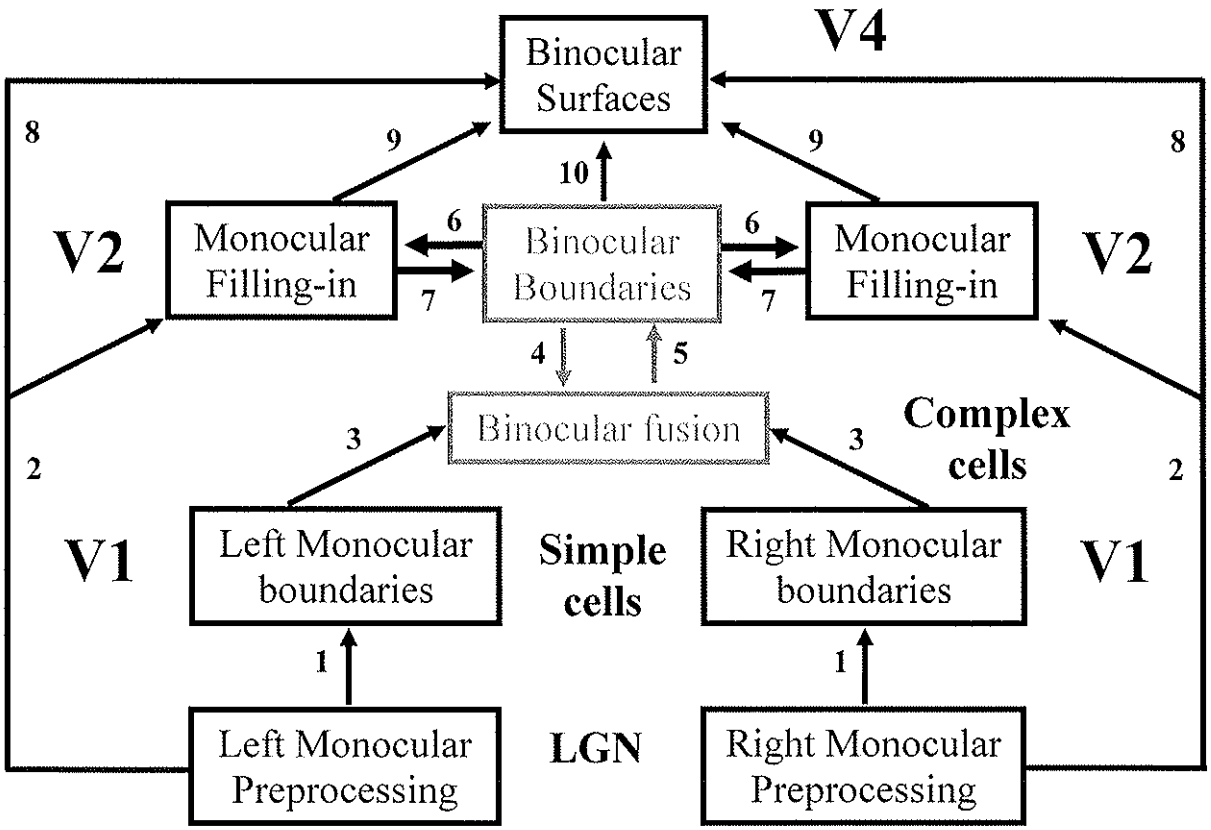

Figure 8. In FACADE theory, the illuminant-discounted inputs from Right and Left Monocular Preprocessing stage, which is composed of center-surround cells, output to the Left and Right Monocular boundaries composed of simple cells via pathway 1. This is the place where we suggest that like-polarity competition occurs. Via pathway 3, Left and Right Monocular boundaries are binocularly fused and through feedback via pathways 4 and 5 incorporate bipole long-range grouping which is provided by the Binocularly Boundaries Stage. Depthful binocular boundaries mutually interact with the Monocular FIDO stage, where the closed boundaries are filled-in by the illuminant-discounted surface input. The attached boundaries to the successfully filled-in surfaces prune the corresponding boundaries at the farther depths at the same spatial positions. In the binocular FIDO, the Left and Right Monocular Preprocessing stages, and also the Left and Right monocular FIDOs, are matched binocularly (pathways 8 and 9). The former match is an excitatory input to the Binocular Surfaces stage and the latter match is inhibitory and carries out surface pruning. Successful binocular boundaries are added to the same positions from near depths to far depths (pathways 10) to realize boundary enrichment. Due to surface pruning, the illuminant-discounted surface inputs associated with the enriched boundaries are pruned from the depth where boundaries are added (Pathway 9). This final step does not qualitatively change the stratification obtained in the simulation herein through mutual interactions between pathways 6 and 7. However, for complete occlusion cases, this final Binocular FIDO stage is critical. Otherwise, the completely occluded object can be seen through the occluder, which will then wrongly be considered transparent (see Grossberg (1994, 1997) for further discussion). The simulations in Figures 15 and 18 illustrate all of these processing stages.

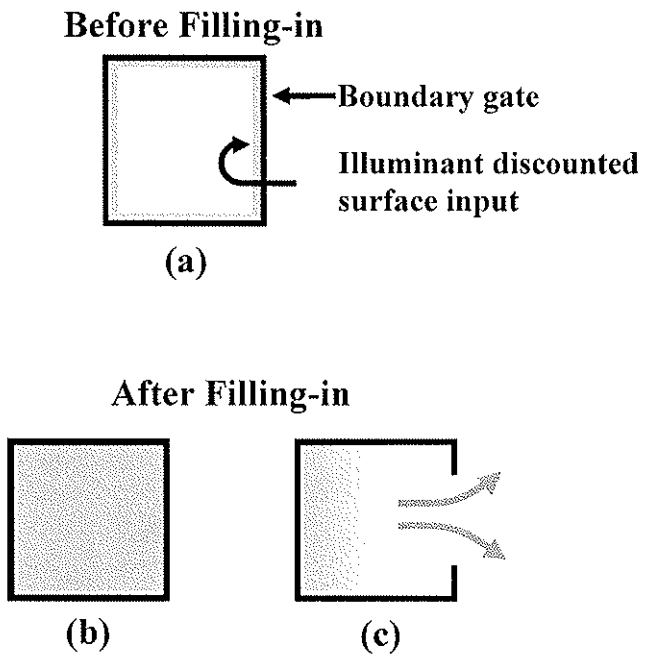

Figure 9. Each boundary output to the surface filling-in system is accompanied by illuminant-discounted surface inputs which estimate the contrast magnitude across the corresponding edge. (a) Before filling-in. (b) If the boundary does not have a gap, it then can contain filling-in and may lead to a visible surface percept. (c) A boundary with gap lets the filling-in process dissipate, thereby preventing a visible surface percept.

9. How can surface interaction with boundary grouping cause transparency?

In FACADE theory, a surface with a connected boundary is represented at a nearer depth than one with a boundary gap (Figures 10). This property depends upon the fact that, in response to viewing a 2D picture, image boundaries initially form in several depth planes, due to the size-disparity correlation (Kulikowski, 1978; Richards and Kaye, 1974; Schor and Tyler, 1981; Schor and Wood, 1983; Schor, Wood, and Ogawa, 1984; Tyler, 1975, 1983). A closed connected boundary in the BCS can contain filling-in within its surface region in the FCS. A contrast-sensitive network within the FCS can then be activated at the edges of this region. This network sends feedback from the FCS to the BCS. The feedback is *positive* to the boundary at its depth and *negative* to boundaries at the same positions but further depths (Figure 11a). This FCS-to-BCS feedback confirms and strengthens the boundary that formed the surface region, while it inhibits, or prunes, extra boundaries that are formed due to the size-disparity correlation (Figure 11b). In so doing, it assures the consistency of boundary and surface representations. The inhibition by near surfaces of far boundaries is called the *asymmetry between near and far*.

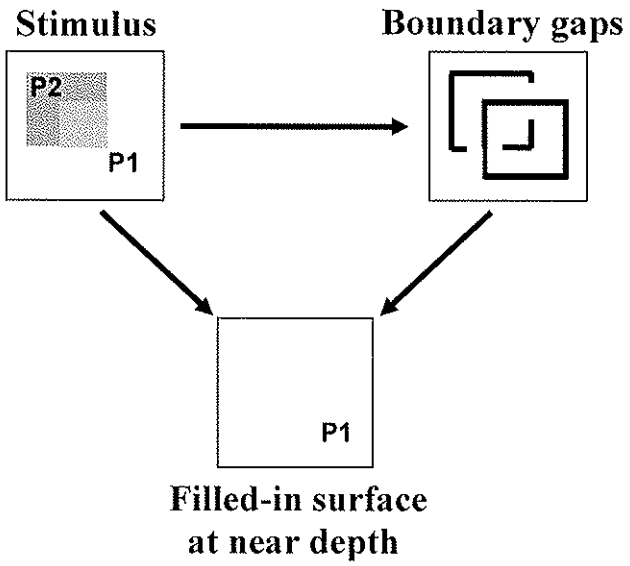

Figure 10. In response to the stimulus the intact boundary keeps its surface at the near depth and the surface presentation of the broken boundary will be forced behind (see the next Figure).

When the boundaries of the near surface are inhibited, the boundary gaps in the next depth can be removed by collinear grouping, and the resultant closed boundary can contain surface filling-in of its illuminant-discounted input (Figure 11b). The filled in surface at the far depth includes the overlapping region of the two squares, meaning that the overlapping region in the image is represented in both near and far depth planes (Figure 11b). Here the contrast is stratified into two separate depths of surface representation, which corresponds to the percept of transparency. This outcome can also be rephrased as filling in of the far depth surface, behind the near depth surface which is equivalent to the near surface transparency.

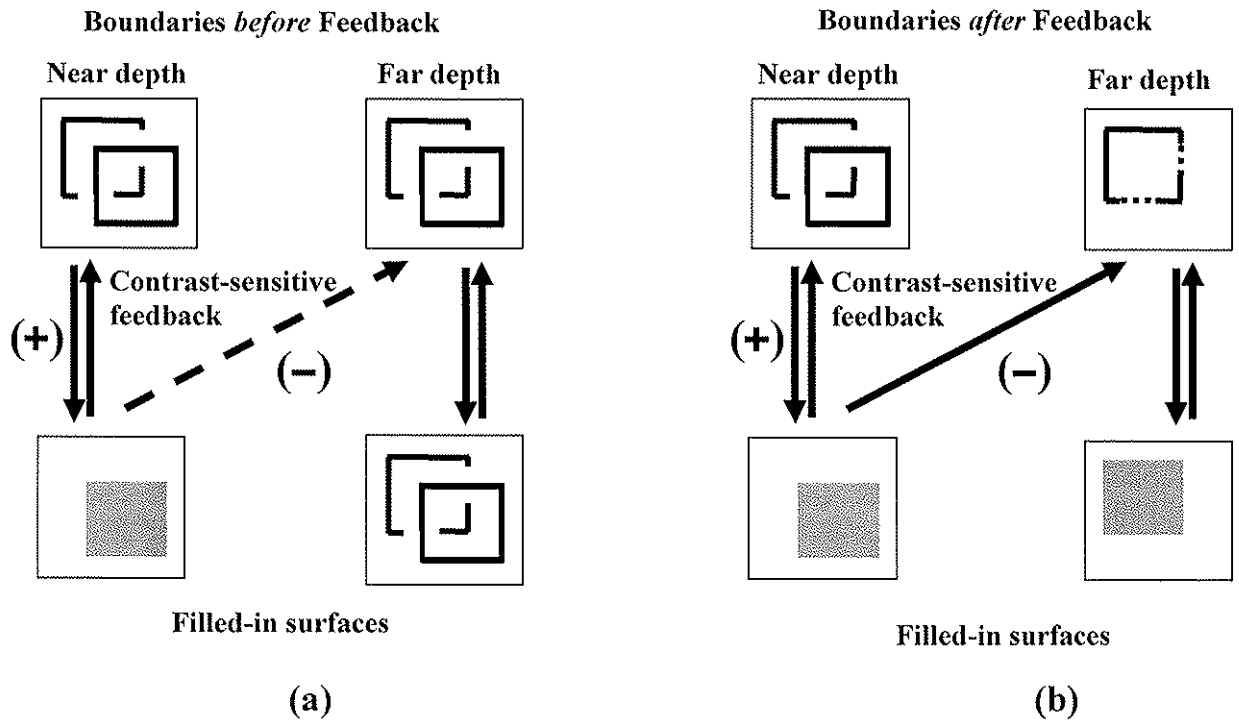

Figure 11. (a) Upper row shows that the initial boundary grouping is redundantly represented at several depths due to size-disparity correlation. The successfully filled-in region will be assigned to the nearest depth that can create a closed connected boundary. Further boundaries at these positions are inhibited by contrast-sensitive topographic feedback from the successfully filled-in surface region. (b) Contrast-sensitive inhibitory feedback prunes the boundaries at further depths while strengthening the successfully filled-in boundaries at the near depth. Gaps in the occluded boundaries can then be repaired by collinear grouping.

One discriminative feature of FACADE theory with regard to surface presentation is: Binocular surface formation stage (Figure 8) discriminates between partial occlusion (transparency) and total occlusion. This is done by adding the attached boundaries of the successfully filled-in near surface to the far depths and pruning their corresponding monocular surface input from the far depth. This process blocks the filling-in of a surface under total occlusion behind the occluder. In the present article, all of the stimuli have partial occlusion or may give rise to neon spreading. Therefore the results of the binocular surface representation in V4 should be consistent with the stratification already obtained from the surface and boundary interactions at V2. Our simulation results confirm this fact (Figure 15b and c) and we will discuss the related results in Section 14.1. The above discussion shows how boundary gaps can lead to a transparent surface percept. The next section shows how the monocular contrast constraint enables these gaps to form, and how they are repaired.

10. How are boundary gaps created and repaired?

Perceptual grouping takes place in layer 2/3 of V2 (Figure 7). The *bipole property* of such groupings can both generate boundary gaps and repair them. Two key properties of the bipole grouping kernel are shown in Figure 12; namely, long-range excitatory horizontal connections

and short-range inhibitory connections located in layer 2/3 of V2 (Figure 7). The excitatory connections that converge on a bipole cell from opposite sides enable it to complete illusory contours at positions that receive no bottom-up input. The inhibitory connections prevent such a boundary from forming unless there is convergent excitatory input from both sides. These inhibitory interactions also compete with boundaries that are trying to form with different, notably perpendicular, orientations at the same position. We will see below how the monocular contrast constraint assures that the boundaries of the rightmost square in Figure 12a are stronger than those of the leftmost square. After competition (Figure 12b), the boundaries of the leftmost square are broken (Figure 12a). When contrast-sensitive feedback prunes the redundant boundaries of the rightmost square from the far depth (Figure 11b, far depth), the bipoles at the far depth no longer receive competition from the rightmost square. They can then collinearly complete the boundaries of the leftmost square (Figure 12c and 12d), which can then trigger filling-in of this square (Figure 11b), thereby leading to a percept of unique transparency.

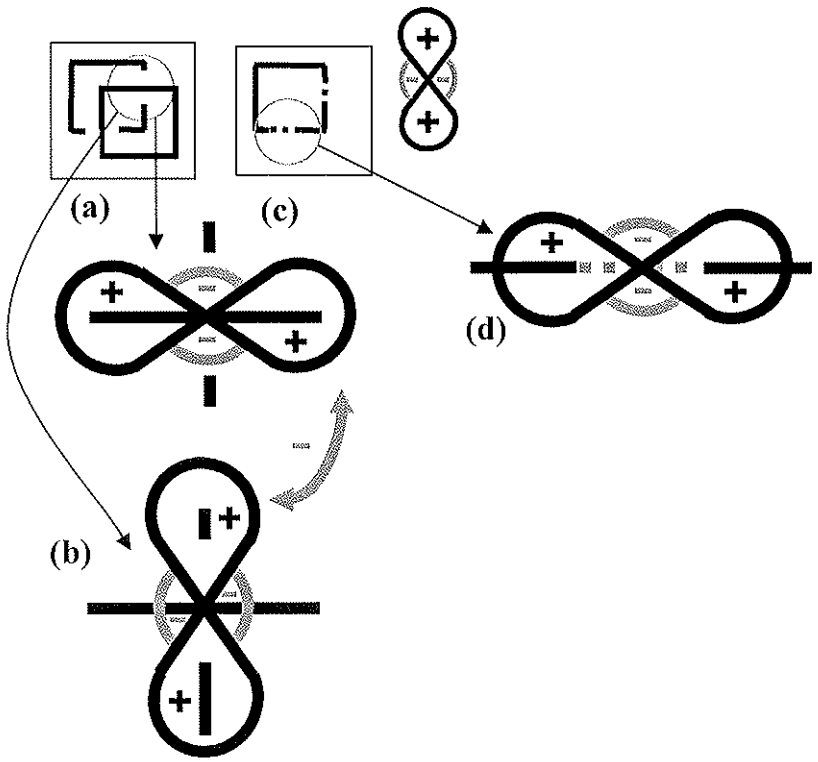

Figure 12. How boundary gaps are generated and repaired? Panel (a) shows that in the unique transparency, the underneath surface boundaries get gaps (within the circle) and as soon as boundary signal across the gap is pruned the gaps can be repaired (see inside the circle). Panel (c) which is the zoom in of the circle region of panel (a) shows how gaps can be created: The bipole grouping cells with different orientation preference (here orthogonal) compete. The stronger boundary inhibits the weaker one bipole grouping through orientational competition and causes gaps. The circle zone in (b) can be repaired because both lobes of bipole grouping cells get input (d). However, the orthogonal boundary signal across the gap blocks the bipole grouping (e) both due to the activation of the inhibitory part of the bipole and also orientational competition as in (c).

11. Bipole grouping is not sufficient

Why are the boundaries of the rightmost square in Figure 12 stronger than those of the leftmost square? The unique transparency image shown in Figure 13 shows that the contrast value at region A is larger than at region B. In addition, the contrast values at C and D can be nearly equal. In these cases, the average contrast of edge AC is larger than that of BD. How, then, does the bipole whose lobes are on BD win over those on AC, as required by Figures 11 and 12?

Something more must happening to generate the proper boundary gaps, other than bipole grouping. Although the average contrast of edge AC is larger than that of BD, the contrast polarity of edge A is the same as that of the edge C, whereas the contrast polarities of B and D are opposite. Monocular polarity-specific competition therefore weakens the AC boundary, but not the BD boundary. As shown below, the competition weakens the amplitudes of inputs to the AC bipoles, but not the BD bipoles. This additional property, when combined with the other properties summarized in Figure 11 and 12, suffices to explain all of our targeted data.

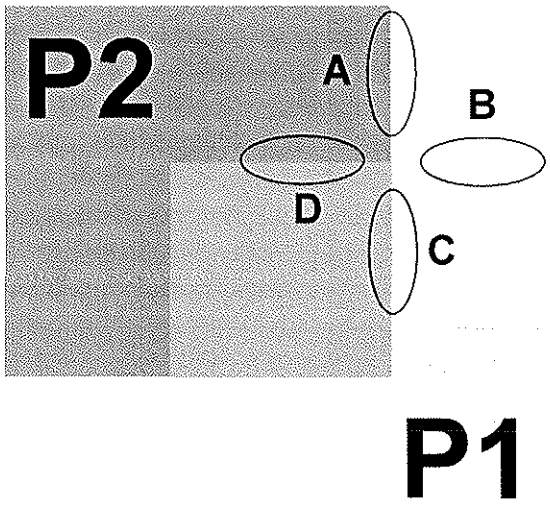

Figure 13. Boundary BD wins over AC even if contrast AC > BD to keep the transparent surface in front. While contrast A is larger than B, in many cases, contrasts D and C can be on the same order which results in contrast AC > BD. Consider Figure 15 for the solution of this "absolute value problem"

12. Prediction: Monocular polarity-specific competition occurs in V1 layer 4

We propose that the monocular polarity-specific competition occurs between simple cells of layer 4. Each layer 6 simple cell in Figure 7 directly excites the corresponding layer 4 simple cell with the same contrast polarity and indirectly inhibits it via the inhibitory interneuron. Because excitation and inhibition are approximately balanced within the on-center of the layer 4 cell, with the excitation possibly a little stronger, net excitatory modulation by layer 6 of layer 4 can occur. The layer 4 cell is activated to suprathreshold values by direct LGN inputs. In addition, off-surround inhibition from layer 6 to layer 4 extends to the coaxial flankers of layer 4 simple cells that have the same polarity response. This circuit is proposed to embody the monocular polarity-specific competition.

In particular, in the unique transparency stimulus of Figure 13, A and C have the same contrast polarity, hence they compete, so the simple cell activities in this region become weaker. Because regions B and D have opposite contrast polarity, they do not compete. Their corresponding simple cell activities not only remain strong, but are actually stronger than in the case that either boundary B or D would have continued uniformly without crossing a junction. This is because a uniform edge has the same polarity of contrast along its border, which activates the same-polarity competition pathway. The reversal of polarity from B to D frees the corresponding simple cells from continuous edge-induced inhibition and thereby makes the boundary signal around the junction zone stronger than in the case wherein the uniform edge continues. Now the strong BD boundary can win over the weakened AC boundary at the bipole cells in V2, despite the fact that the average absolute contrast of AC is greater than that of BD. The Results section will also show that these mechanisms correctly stratify the bistable and nontransparent cases.

The same mechanisms are sufficient to explain data about neon color spreading or blockade. Figure 14a shows that the desired situation is the winning of the bipole grouping along AC over BD even if the contrast value of D is greater than that of A. In many such situations, the average contrast value along BD is greater than AC (note around C, there is no contrastive edge). Monocular polarity-specific competition helps to solve this problem: Boundary A is freed from same polarity-specific competition because it ends after crossing BD, and thereby gets stronger. However, there is polarity-specific competition within BD. The strengthening of the A through discontinuation and the weakening of BD through polarity-specific competition enable the bipoles which form an illusory contour by grouping AC to win over BD through orientational competition.

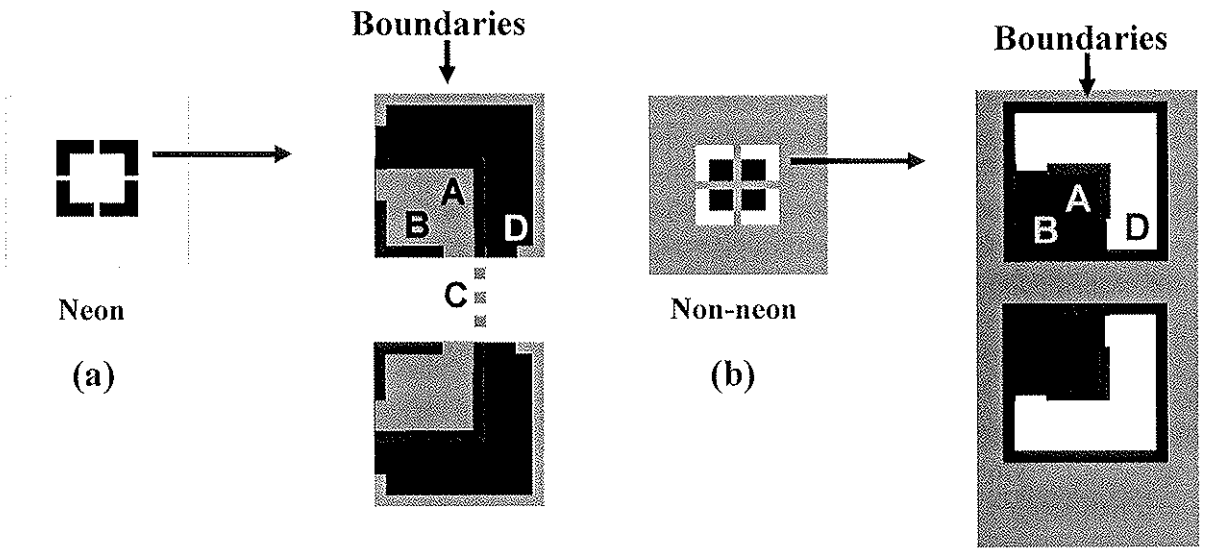

Figure 14. Neon and no-neon cases: Boundary AC can win even when contrast D exceeds contrast A. Polarity-specific competition between B and D allows boundary AC to win. (b) Boundary BD can win even when contrast A exceeds D. Opposite-polarity B and D contrasts do not compete. Boundaries are shown schematically as grey edges.

The same sort of hypothesis can successfully explain the blocked neon case of Figure 14b. Boundary BD can here use its bipole grouping advantage to win even if the contrast value at A is greater than at D. This is because opposite polarities B and D do not compete.

Our prediction for the necessity of the like-polarity competition based on the modeling constraints and indirect psychophysical inference is also consistent with the experimental data of Polat and Sagi (1993), in which the detection threshold of a Gabor patch being flanked with two patches with the same polarity of contrast increases when the flankers get nearer and nearer to the target. In their experiment, the flanker contrasts were in phase with the target contrast, equivalent to a like- polarity condition. It remains to be tested via direct recording in V1 what happens if the flanker contrast and the target contrast are spatially out of phase. One has to be cautious even to draw the conclusion that in the out-of-phase case, or opposite polarity case, the raised threshold effect will be less, because polarity-pooled cells of V2 may modulate in complex ways the predicted V1 spatial competition difference between the in-phase and out-of-phase flanker-target paradigm.

13 Same ocularity of contrast can induce neon

The combination of monocular polarity-specific competition and binocular contrast-invariant bipole grouping can also explain the Tacheichi et al. (1992) data. In the no-neon case of Figure 4, the different ocularity of the contrasts bypasses the monocular polarity-specific competition in V1. The same polarity (gray-white) of the right panel is thus not adjacent to the same polarity (black-white) of the left panel to activate this competition. In the neon case of Figure 3, monocular polarity-specific competition contributes to boundary gap formation in favor of the long-range bipole cooperation that completes the illusory square. The illusory square can form between inducers with different ocularities because layer 2/3 bipole grouping cells in V2 are binocular (Figure 7). Taken together, the endgaps and binocular illusory contours can support the neon effect, as simulated below.

14 Simulation results

14.1 Simulation of unique transparency phenomenon

For simplicity, the present simulations contain only two depth planes: Near and far. 3D LAMINART simulations of 3D planar surface percepts with more depth planes are given in Grossberg and Howe (2003) and illustrate that the present simplification generalizes. Initially, the same boundaries occur in both depth planes (Figure 15a). As described in Figure 11a, the boundary corresponding to the transparent surface edge is intact and that of the underneath one has gaps. Surface filling-in is contained within the connected boundary and flows away through the gaps of the broken boundary. Figure 15a shows the situation before the contrast-sensitive feedback takes place from the connected near surface to the far depth boundaries.

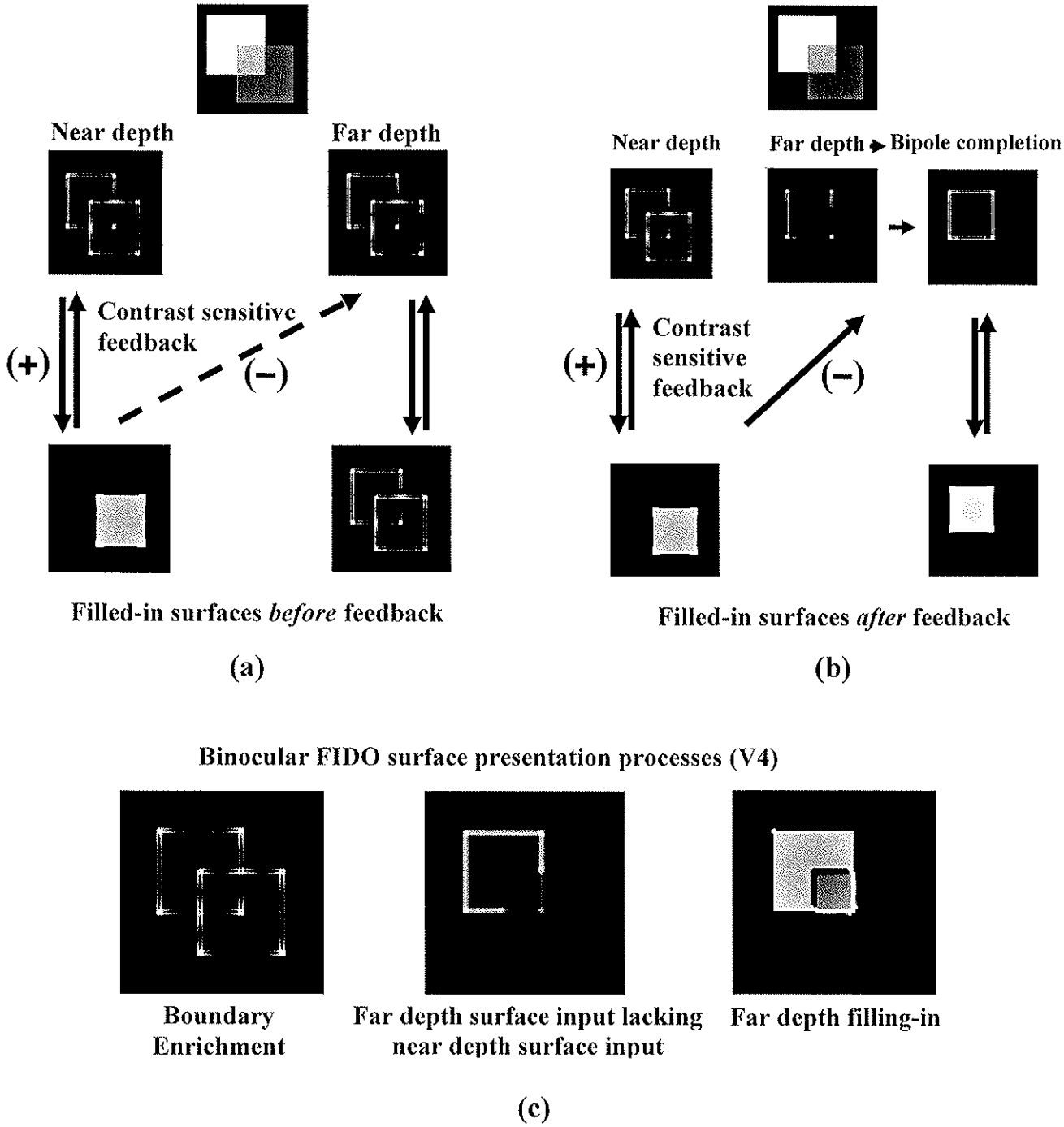

Figure 15. (a) Before boundary pruning occurs from near-to-far, the boundary gaps in the far depth cannot be repaired. (b) After far depth boundary pruning occurs, the repaired gaps close the square boundary and allow it to contain the filling-in process. (c) The binocular FIDO stage (V4) from left to right: The near depth connected boundaries are added to the far depth boundaries. The middle panel shows that the corresponding surface inputs related to the enriched boundaries are pruned from the far depth. The right panel shows the surface filling-in of the far depth. See the text for full description.

Figure 15b shows that the analysis in Figure 11b works; namely, after contrast-sensitive surface-to-boundary feedback, the far boundary of the successfully filled-in near surface is pruned. This frees the bipole grouping kernels to repair the remaining far boundary gaps (Figure 15b). Now surface filling-in at the far depth can be contained in this closed boundary. A transparency percept obtained due to the stratified co-occurrence of surface representations at both depths within the small nested square.

In Figure 15c, the processes involved in the binocular FIDO in V4 are shown. The near depth replicates the boundary and filled-in surface of Figure 15b at the binocular FIDO. However, the situation at the far depth in V4 differs from that in V2. In the leftmost panel, the boundary of the successfully filled-in surface at the near depth is added to the boundary at the far depth (boundary enrichment). In addition, the surface inputs corresponding to the far boundaries are pruned from the far depth (surface pruning). In the rightmost panel, the resultant surface and boundary interaction within the binocular FIDO is shown. As can be seen, the weaker contrast of the lower-right part of the square, and the separation of this part from the rest of the square by the boundary enrichment process, result in a weaker surface activity (rightmost panel of Figure 15c). The latter surface activity is behind the near surface, hence gives rise to the transparency percept again. This weaker contrast illustrates how contrasts can be stratified across multiple depths.

14.2 Bistable transparency simulation

In the bistable transparency case (Figure 1b), both stems of the X-junction preserve polarity, and due to polarity-specific competition, both generate weak boundaries. If the contrasts of both X-junctions are balanced, then their bipoles cannot generate boundary gaps. Where such a balance persists, Figure 1b may result in a non-stratified percept with a small square in the middle and two flanking L shapes. However, if attention shifts between the edges of the X-junction, or their corresponding surface regions, then bistable endgaps and bistable transparency can occur, because attention can favor one of the boundaries. Grossberg and Raizada (2000) and Raizada and Grossberg (2001) have previously modeled how attention can modulate boundary groupings, notably how it can have a larger strengthening effect on weak groupings than on strong groupings (DeWeerd et al., 1999; Raizada and Grossberg, 2003). Our simulation is consistent with their results on how attention modulates weak and strong boundary groupings. The effect of attention is simulated as top-down Gaussian activation to layer 6 of V1 (Figure 16c). Layer 6, in turn, positively modulates layer 4 activation (Figure 16c). The added subliminal activation of layer 4 in favor of any boundary enables it to win the orientational competition and to push its surface to the near depth plane.

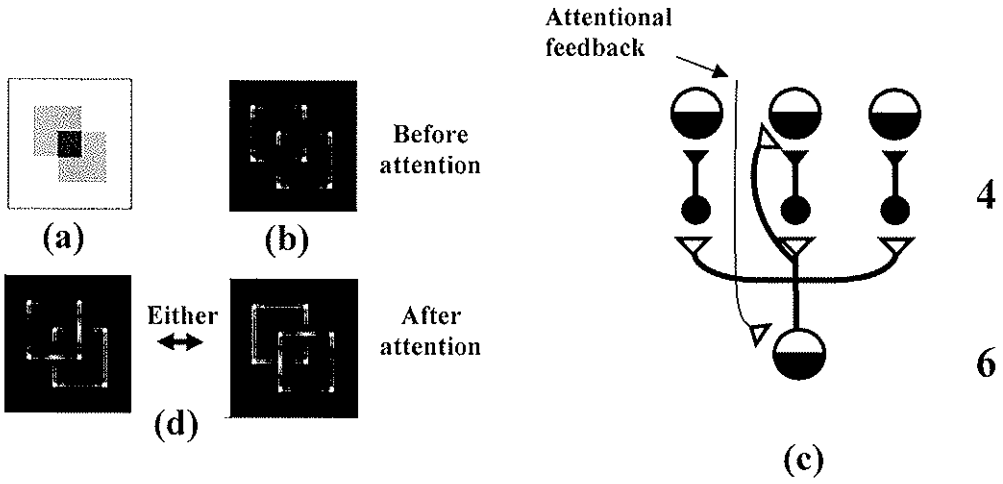

Figure 16. In the bistable transparency case (a), the same polarity along both stems of X-junction makes their boundaries weak and unable to win over the other (b). Positive modulatory attentional feedback (c) to either of the stems makes it win over the other (d). See the text for details.

14.3 Non transparent simulation

A double polarity-reversing X-junction (Figure 1c) generates strong boundary signals around X-junctions. Orientational competition here too cannot generate gaps along either of them. Because both stem boundaries are strong due to the lack of polarity-specific competition, subliminal attentional boundary enhancement in favor of either stem cannot make it win over the other one, consistent with the greater effect of attention on weak than strong groupings.

The illuminant-discounted surface input successfully fills-in all the closed contours, so contrast-sensitive feedback prunes all the boundary copies in the far depth; hence, no boundary signals remain there. All surfaces hereby form in one depth plane with no surface representation behind the overlap region, as shown in Figure 17, so there is no percept of transparency.

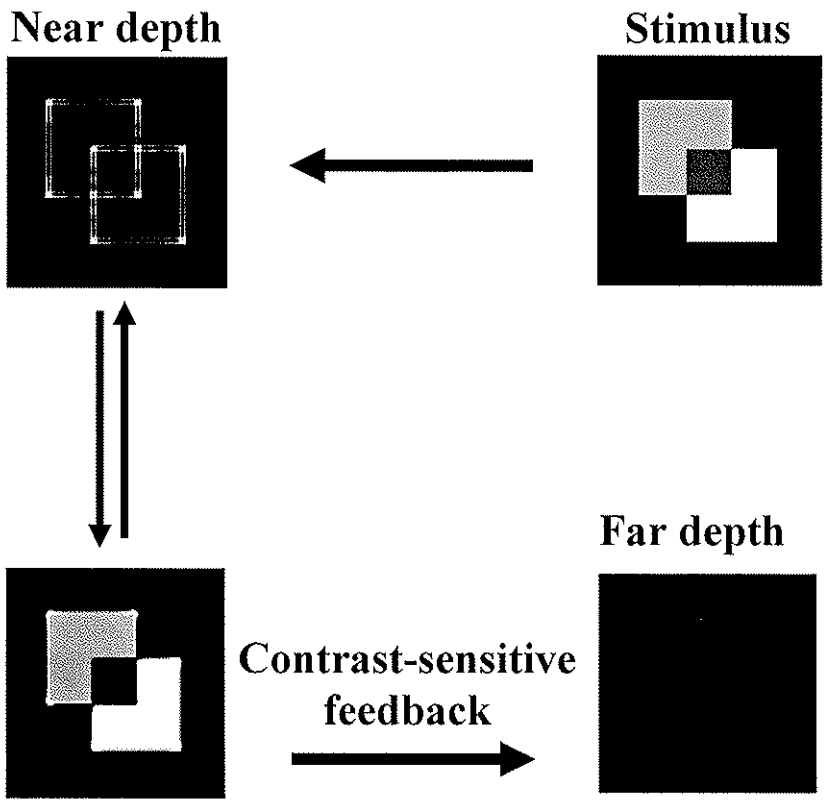

Figure 17. In the non-transparency case, polarity reversal along both stems of X-junction leads to strong boundaries that can resist orientational competition. Attention to either boundary cannot break the other strong stem. Therefore, all closed boundaries are filled-in at the same depth plane. See text for more details.

14.4 Neon simulation

In the neon case of Figures 2a and 18a, polarity-specific competition enables the illusory square to form, as illustrated in Figure 14a. The illusory square interpolates the boundary gaps. A square surface fills-in at the near depth plane, so that contrast-sensitive feedback prunes the square boundary from the far depth plane. Boundary completion can then form four small squares at the far depth plane, which can then fill-in.

The simulation clarifies the perceptual experience that the surface quality of the neon is pretty weak. In the simulation, feature contrasts occur at the four small gray square corner inducers of the illusory square. These sparse inducers spread throughout the entire illusory square. This is unlike the transparency case in which the surface input exists along the whole edge of the square. In the neon case, the illusory parts of the square sides do not have any surface input, because there are no contrastive edges there. In the neon case, only the corner surface inputs spread in the square with illusory sides.

In Figure 18b, the simulation of the binocular FIDO stage is shown. The leftmost panel shows the boundary enrichment at the far depth. The surface inputs corresponding to the near connected boundaries are pruned from the far depth surface input (middle panel). The filling-in of the pruned surface input within the enriched boundary is shown at the right panel. Here again, the far depth surface representation is not different qualitatively at the monocular and binocular

FIDOs, because the small corner square surface inputs are intact at the far depth after surface input pruning.

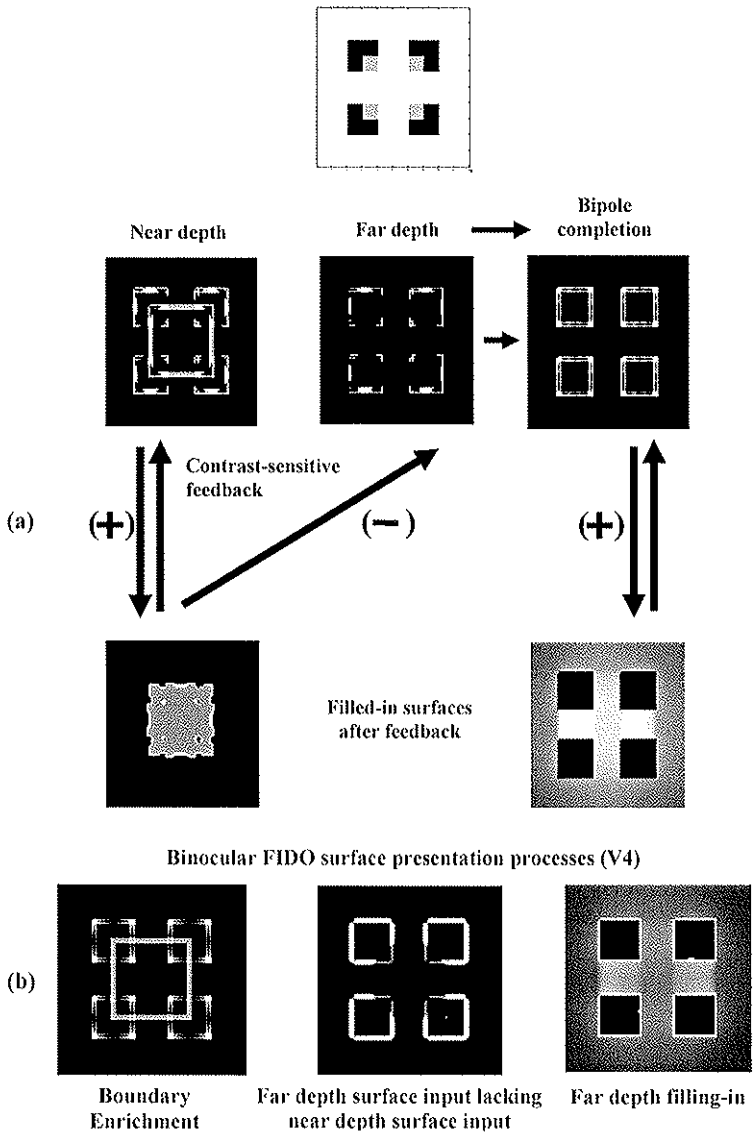

Figure 18. (a) In the neon case, the preserved polarity along the T-junction tops weakens the top boundary signals and enables boundary gaps to form via orientational competition. These gaps create a suitable condition for long-range grouping whereby the middle square illusory boundary forms. This middle square fills-in successfully and after pruning the corresponding boundaries from the far depth, four small square boundaries are repaired by long-range grouping after being released from orientational competition by the middle square boundaries. Filling-in of the four squares can then occur behind the middle square. (b) Left panel shows that, at the binocular FIDO stage, the connected boundaries of the successfully filled-in surface at near depth are added to the boundaries at the far depth (boundary enrichment). The surface inputs corresponding to the enriched boundaries are removed from far depth via surface pruning (middle panel). The surface filling-in within the enriched boundaries by the pruned surface input represents the four corner squares at the far depth (right panel).

14.5 Non-neon simulation

Figure 19 shows the effect of polarity reversal along the T-junctions in strengthening the boundaries corresponding to the top of the T-junction, and in not allowing the perpendicular bipole grouping to take place, as schematized in Figure 14b. As a result, the whole surface representation is on one depth plane. In this regard, it is similar to non-transparent simulation in Figure 17.

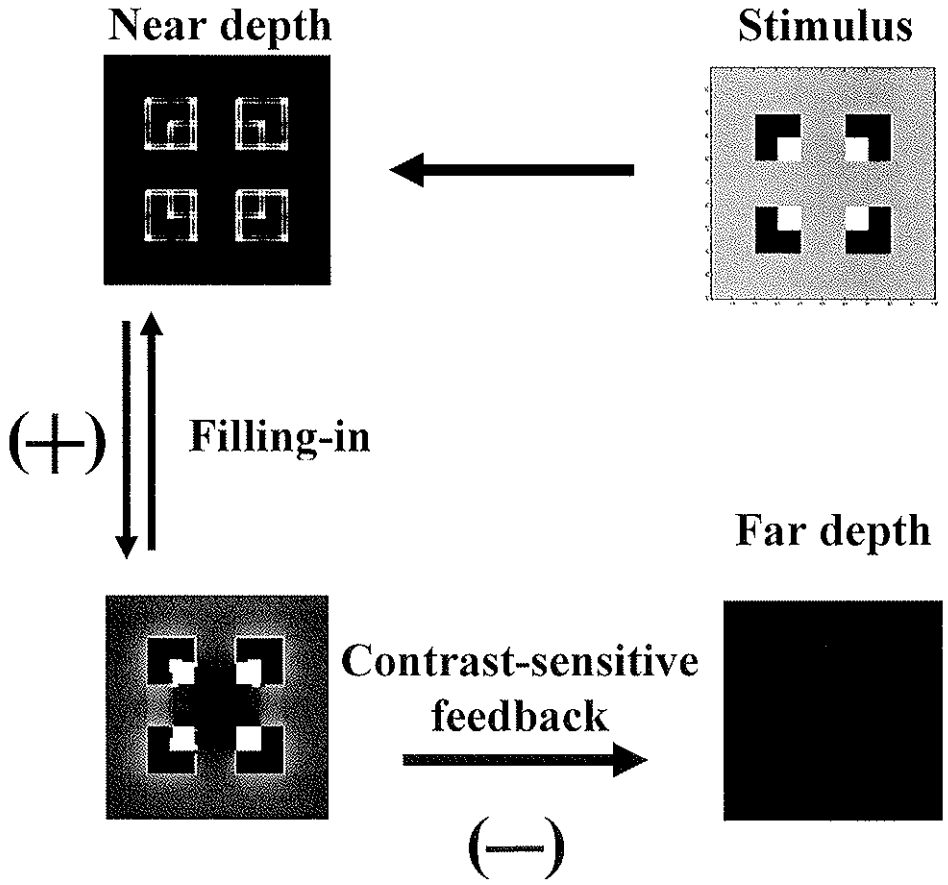

Figure 19. In the non-neon case, opposite polarities along the tops of the T-junctions strengthen the top boundaries, which in turn block the long-range grouping by orientational competition.

14.6 Dichoptic neon simulation

In the neon split case (Figure 3) because the whole contrast exists within each monocular inducer, suitable boundary gaps will be generated and binocular long-range grouping can bridge between inducers with the opposite ocularity (Figure 20). The rest of the process is the same as in the neon case of Figure 18.

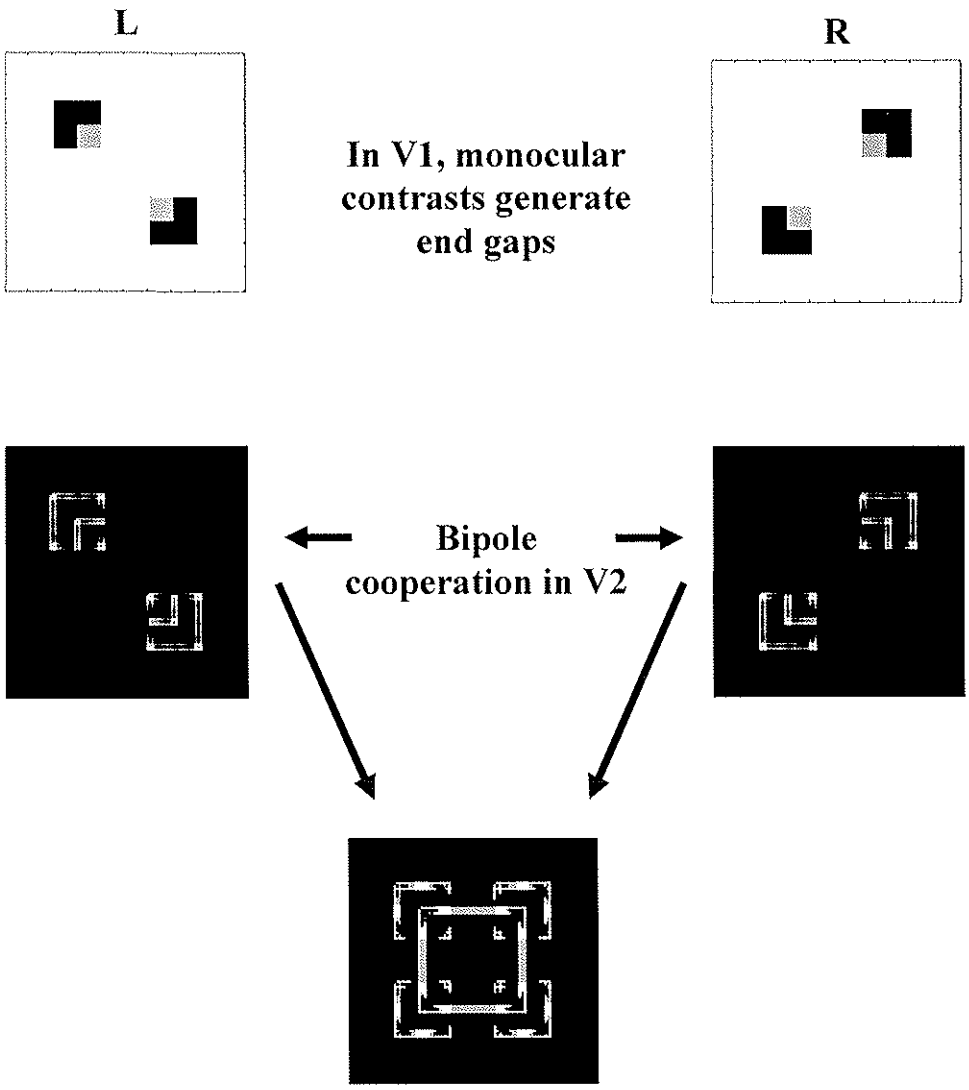

Figure 20. In the dichoptic neon case, the presentation of the whole contrast to each eye generates boundary endgaps. Due to the binocularity of long-range grouping, the middle illusory square boundary can form. Hence neon can be generated. See text for details.

14.7 Dichoptic non-neon split contrast simulation

Due to the different ocularity of the contrast components in this case (Figure 4), the boundaries especially around the line ends get stronger. The pooling of polarity and ocularity at layer 2/3 of V2 results in strong boundary signals perpendicular to the orientations of the illusory square that forms in the neon case. Orientation competition prevents boundary gaps and illusory contour formation from occurring (Figure 21).

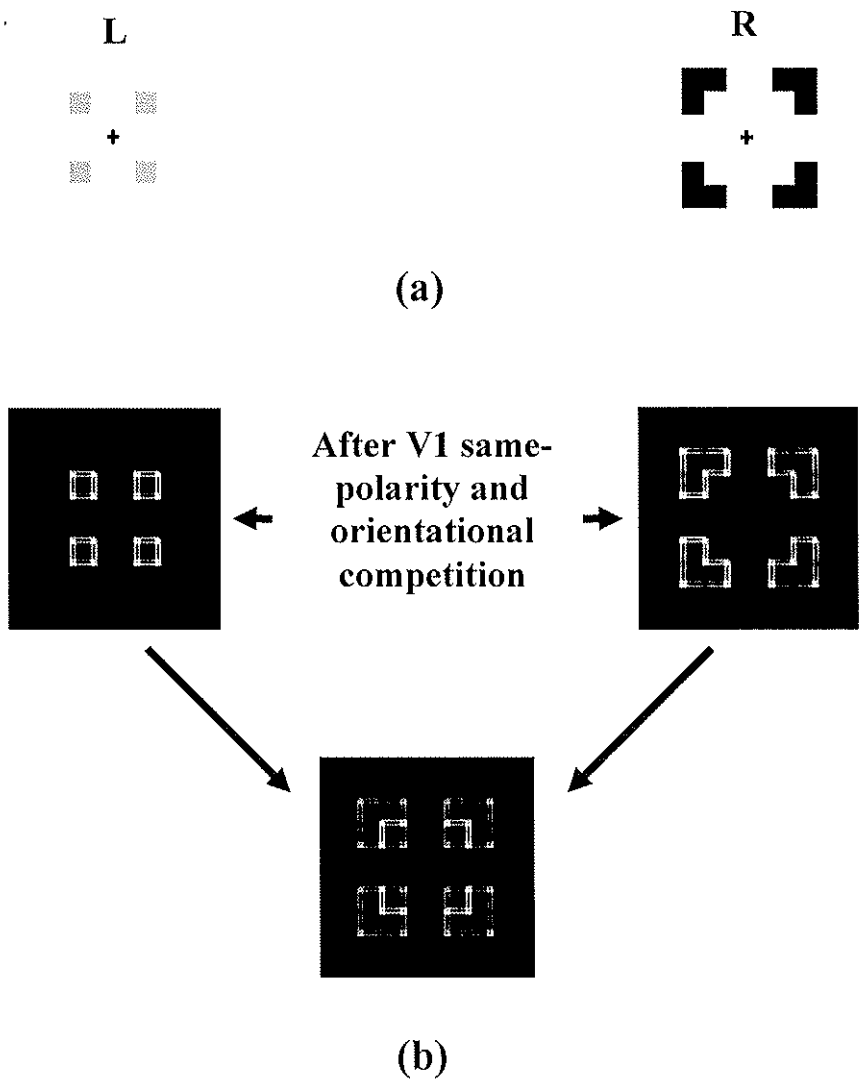

Figure 21. In the dichoptic non-neon case, the different ocularity of the contrast components (a) bypasses the polarity-specific competition so that no endgaps are formed (b). Binocular long-range grouping to form a middle illusory square is blocked by strong perpendicular boundaries (b). See text for details.

15. Discussion

The stimuli that generate transparency and neon color spreading are rare in natural conditions. Many of them exist just in experimental setups and are not among the most common stimuli reaching our visual system. However, they illuminate constraints on visual system strategies for depth stratification that have evolved in natural environments. These constraints suggest that the like-polarity constraint on contrast has its effect in monocular configurations. This idea, coupled with previous modeling results, leads to the prediction that this constraint is realized in the

monocular circuits of layers 6 and 4 of V1. A second constraint is that long-range grouping must be possible in response to dichoptic inputs. This is consistent with the binocular bipole grouping that is proposed by the 3D LAMINART model to take place in layer 2/3 of V2. Third, it was shown that how the laminar organization of cortical circuits helps to separate the contrast-sensitive competitive filtering process and contrast-invariant cooperative grouping process. Fourth, after characterizing the effect of these competitive and cooperative effects on boundary formation, we saw how the interactions between the boundary formation and surface filling-in systems which are postulated in FACADE gave the correct stratification results in all the neon and transparency cases.

When the like-polarity constraint is realized within the 3D LAMINART model, it provides a mechanistic explanation of the classical Metelli rules for when a transparent percept will be generated. In particular, Beck, Prazdny, and Ivry (1984) and Metelli (1974) showed that the impression of transparency occurs when (1) "the overlying of the transparent surface does not change the order of the lightness values", and (2) "the lightness difference within the transparent area must be less than the lightness difference outside the transparent area". Because of the like-polarity competition, constraint (1) is enough to break the boundary of the non-transparent surface and leave that of transparent one intact. Like-polarity competition supplemented by orientational competition generates a larger gap on the boundary of non-transparent surface inside the transparent area than outside of it if constraint (2) is obeyed. The larger gap leads to a more uniform spreading of surface activity within the transparent area. This is consistent with our perceptual experience: The overlaying transparent surface has a uniform surface quality.

The contrast-invariant binocular long-range grouping process in layer 2/3 of V2 has a clear ecological value; see Figure 6 and Grossberg (1994). Can the same be said for monocular polarity-specific competition in layer 6-to-4 of V1? Earlier analysis have shown that the layer 6-to-4 competition has at least three important functions (Grossberg, 1999a): (1) It contrast-normalizes the responses of layer 4 cells to bottom-up inputs; (2) it assures that the correct groupings are selected via layer 2/3-6-4-2/3 feedback without losing their analog sensitivity to inputs; and (3) it maintains an approximate balance between excitation and inhibition in the layer 6-to-4 on-center that enables top-down attention to modulate layer 4 cells, as in Figure 16c. These properties do not, however, require the polarity-specificity of layer 4 competition. How does this constraint arise? Grossberg and Williamson (2001) simulated how the layer 6-to-4 competition and the layer 2/3 long-range grouping connections develop. Their study showed how the approximate balance between excitation and inhibition in the layer 6-to-4 on center could develop. This result supported an early prediction from Adaptive Resonance Theory, or ART, that feedback via a modulatory on-center off-surround network is needed to dynamically stabilize cortical development and learning (Grossberg, 1980, 1999b). The simulation of Grossberg and Williamson (2001) showed that, if the excitation or inhibition got too strong, then model development did not stabilize.

The developmental and learning laws that achieved the desired stabilizing balance also led to an inhibitory kernel around layer 4 cells that links cells which code the same collinear orientation, as a manifestation of the heuristic rule "cells that fire together wire together". Under natural viewing conditions during which, with high probability, objects have the same contrast polarity for a considerable distance along their edges, one would expect monocular polarity-specific inhibitory kernels to develop.

This analysis leads to new experimental questions and predictions: In particular, what happens to these inhibitory kernels if animals are reared in an artificial environment composed of

textures whose polarities reverse at frequent intervals across space? Do the animals develop inhibitory kernels that violate the polarity-specific constraint? Do they see transparency and neon percepts differently than we do?

Appendix: 3D LAMINART Equations

In the LAMINART circuit shown in Figure 7, total excitatory and inhibitory inputs to each cell can be represented, respectively, by time-varying conductances $\gamma_{ex}(t)$, and $\gamma_{inh}(t)$ in a membrane equation with a constant leakage conductance γ_{leak} (voltage-independent conductance equal to: $\frac{1}{\text{Resistence}}$) and reversal potentials for excitation E_{Ex} (corresponding to Na^+ channels), inhibition E_{Inh} (corresponding to K^+ channels), and leakage (E_{Leak}). Then the membrane potential $V(t)$ can be written as:

$$C\frac{dV(t)}{dt} = -[V(t) - E_{Ex}]\gamma_{Ex}(t) - [V(t) - E_{Inh}]\gamma_{Inh}(t) - [V(t) - E_{Leak}]\gamma_{Leak}(t), \quad (1)$$

where C is the conductance of the cell membrane.

In many parts of the simulation, (1) is solved at equilibrium. At equilibrium, the above equation becomes:

$$V = (E_{Ex}\,\gamma_{ex} + E_{Inh}\,\gamma_{inh} + E_{Leak}\,\gamma_{inh}) / (\gamma_{ex} + \gamma_{inh} + \gamma_{inh}). \quad (2)$$

The denominator in (2) shows how the membrane potential is normalized divisively. In the subsequent simulations, $E_{Ex} = 1$, $E_{Inh} = -1$, $E_{Inh} = 0$, $\gamma_{ex}(t)$ and $\gamma_{inh}(t)$ are replaced by total excitatory and inhibitory signals, respectively. The resultant differential equations are then solved either in equilibrium or by the forward Euler method with the time step of 0.05 ms in MATLAB. The surface filling-in simulations are written in C++ as a MEX file incorporated into MATLAB to make the run time faster. Equations that were solved at equilibrium are written below in the form (2).

A1. LGN input to cortical simple cells

Notation $I_{pq}^{L/R}$ denotes visual output to V1 from LGN cells that are sensitive to the left (L) or right (R) eye at location (p,q). Notation $S_{ijk}^{L/R}$ denotes the oriented and polarity-sensitive input to V1 from LGN, at V1 position (i,j) and orientation k, originating from the left or right eye:

$$S_{ijk}^{L/R} = [\sum_{pq} I_{pq}^{L/R} D_{pqij}^{(k)}]^+. \quad (3)$$

Orientation indices k = 1, 2, 3, 4 (1 and 3 for vertical orientations, and 2 and 4 for horizontal orientations with opposite contrast polarity). Kernel $D_{pqij}^{(K)}$ is defined by a difference-of-shifted-Gaussians:

$$D_{pqij}^{(k)} = G_{pq}(i - \delta\cos\theta_k, j - \delta\sin\theta_k, \sigma) - G_{pq}(i + \delta\cos\theta_k, j + \delta\sin\theta_k, \sigma), \quad (4)$$

with

$$G_{pq}(i,j,\sigma) = \frac{1}{2\pi\sigma^2}\exp\left(-\frac{1}{2\sigma^2}((p-i)^2 + (q-j)^2)\right), \quad (5)$$

where σ =4, δ =2, and $\theta_k = \frac{\pi}{2}(k-1)$, k = 1, 2, 3, 4.

A2. Layer 6 of V1

Cell activity $x_{ijk}^{(1,L/R)}$ of layer 6 of V1 at position (i,j) with left/right (L/R) ocularity and orientation index k is given by:

$$\frac{d}{dt}x_{ijk}^{(1,L/R)} = -x_{ijk}^{(1,L/R)} + (1 - x_{ijk}^{(1,L/R)})(S_{ijk}^{L/R} + \sum_{pq} A_{ij}^{pq}). \tag{6}$$

The attentional feedback term $\sum_{pq} A_{ij}^{pq}$ in (6) is defined by the summation of Gaussian kernels.

$$A_{ij}^{pq} = \frac{1}{2\pi\sigma^2}\exp\left(-\frac{1}{2}\left(\frac{(p-i)^2 + (q-j)^2}{\sigma^2}\right)\right). \tag{7}$$

Attention is used only in the bistable transparency case; see Figure 16. In cases with no attentional feedback, $A_{ijk}^{pq} = 0$. In the bistable transparency case, attention is focused at positions (p,q) which are along either stem of X-junctions. At equilibrium, (6) becomes:

$$x_{ijk}^{(1,L/R)} = \frac{S_{ijk}^{L/R} + \sum_{pq} A_{ij}^{pq}}{1 + S_{ijk}^{L/R} + \sum_{pq} A_{ij}^{pq}}. \tag{8}$$

In both (6) and (8), $x_{ijk}^{(1,L/R)}$ is contrast-polarity sensitive.

A3. V1 layer 4: Monocular simple cells

The monocular simple cell activity of layer 4, $y_{ijk}^{(1,L/R)}$ is given by:

$$\frac{d}{dt}y_{ijk}^{(1,L/R)} = -y_{ijk}^{(1,L/R)} + (1 - y_{ijk}^{(1,L/R)})(S_{ijk}^{L/R} + \eta x_{ijk}^{(1,L/R)}) - (y_{ijk}^{(1,L/R)} + 1)\sum_{pq\in N_{ij}} W_{pqijk} m_{pq}^{L/R}, \tag{9}$$

where η=3. The LGN and layer 6 activate layer 4 through terms $S_{ijk}^{L/R}$ and $\eta x_{ijk}^{(1,L/R)}$, respectively.

The activity of inhibitory interneurons $m_{pq}^{L/R}$ connecting layer 6 to layer 4 of V1 is passed through an elongated Gaussian kernel W_{pqijk}:

$$W_{pqijk} = \frac{1}{2\pi(\sigma_1^2 + \sigma_2^2)}\exp\left(-\frac{1}{2}\left(\frac{(p-i)^2}{\sigma_1^2} + \frac{(q-j)^2}{\sigma_2^2}\right)\right). \tag{10}$$

For the vertical orientation (k = 1, 3), σ_1 = 10 and σ_2 =1, which defines a vertical elongated receptive field. For the horizontal orientation (k = 2, 4), σ_1 = 1 and σ_2 =10, and the interlayer connection is elongated horizontally. The shape of the kernel W_{pqijk} for the vertical orientation (k=1, 3) is shown in Figure A1a.

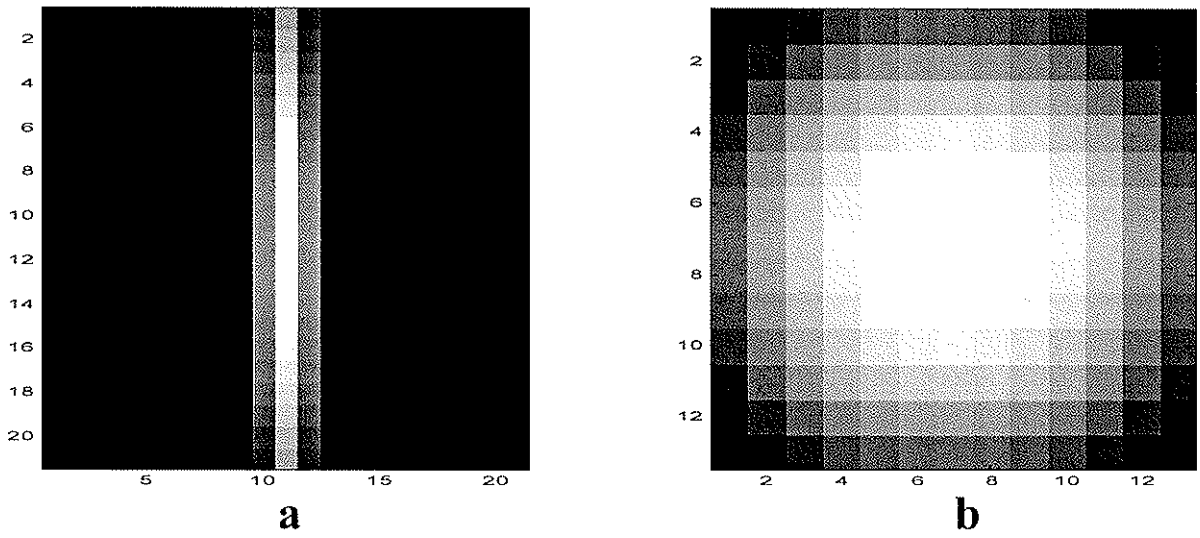

Figure A1

Equation (9) implements the like-polarity competition between the layer 4 simple cells of V1, because the same index k on both sides of (9) restricts the competition to the same orientation and polarity. At equilibrium, (9) becomes:

$$y_{ijk}^{(1+L/R)} = \frac{S_{ijk}^{(L/R)} + \eta x_{ijk}^{(1,L/R)} - \sum_{pq \in N_y} W_{pqijk} m_{pq}^{(L/R)}}{1 + S_{yk}^{(L/R)} + \eta x_{ijk}^{(1,L/R)} + \sum_{pq \in N_y} W_{pqijk} m_{pq}^{(L/R)}}. \tag{11}$$

The inhibitory interneuron activity $m_{ijk}^{L/R}$ follows the equation:

$$\frac{d}{dt} m_{ijk}^{L/R} = -m_{ijk}^{L/R} + \eta^{-} x_{ijk}^{(1,L/R)} - m_{ijk}^{L/R} \sum_{pq \in N_y} W_{pqijk}^{-} m_{pq}^{L/R}. \tag{12}$$

Kernel W_{pqijk}^{-} is a linearly scaled version of W_{pqijk} in (10); namely, $W_{pqijk}^{-} = 0.15 W_{pqijk}$. Equation (12) implements the property that inhibitory interneurons inhibit each other to normalize the total inhibition. The importance of this property was described in Grossberg and Raizada (2000).

A4. V1 layer 3B: Vertical binocular simple cells

The vertically oriented layer 3B cells with activity $b_{ijkd}^{(1,B)}$ (k=1 or 3) binocularly fuse inputs from layer 4 vertically oriented monocular simple cells that are sensitive to the same polarity of contrast. In equilibrium, $b_{ijkd}^{(1,B)}$ is determined by:

$$b_{ijkd}^{(1,B)} = \frac{1}{\gamma_1}\left([y_{(i-s)jk}^{(1,R)}]^{+} + [y_{(i+s)jk}^{(1,L)}]^{+} - \alpha\left([q_{ijkd}^{L}]^{+} + [q_{ijrd}^{L}]^{+} + [q_{ijrd}^{R}]^{+} + [q_{ijkd}^{R}]^{+}\right)\right), \tag{13}$$

where α =5 and γ_1 = 8.5. The obligate simple cell $b_{ijkd}^{(1,B)}$ is excited by layer 4 simple cells of both ocularities with the same polarity (index k in $y_{(i-s)jk}^{(1,R)}]^{+} + [y_{(i+s)jk}^{(1,L)}]^{+}$). Index d shows the depth plane, d = 1 for the near depth and d =2 for the far depth. The parameters i+s and i-s indicate the shifted monocular positions corresponding to the binocular positions i in each depth plane. As can be seen in Figure A2, the retinal images of both eyes can be projected back along the line of

sight onto the fixation plane (d = 1, Figure A2). There, these retinal images match correspondingly. Following the retinal images along the lines of sight onto the far depth plane is associated with horizontal displacement of corresponding retinal images. This horizontal shift, compared to the corresponding position on the fixation plane and dependent on the depth plane and the eye of origin, is called an allelotropic shift and its amount is shown by index s. For d = 1 (near depth, fixation plane in Figure A2), s =0. For the far depth (d = 2), s = 3. The direction of allelotropic shift is opposite for opposite ocularities. Therefore the horizontal coordinates of left and right monocular excitatory inputs from layer 4 to 3B is shifted oppositely (+s and –s in $[y^{(1,L)}_{(i+s),jk}]^+$ and $[y^{(1,R)}_{(i-s),jk}]^+$ on the right hand side of (13)).

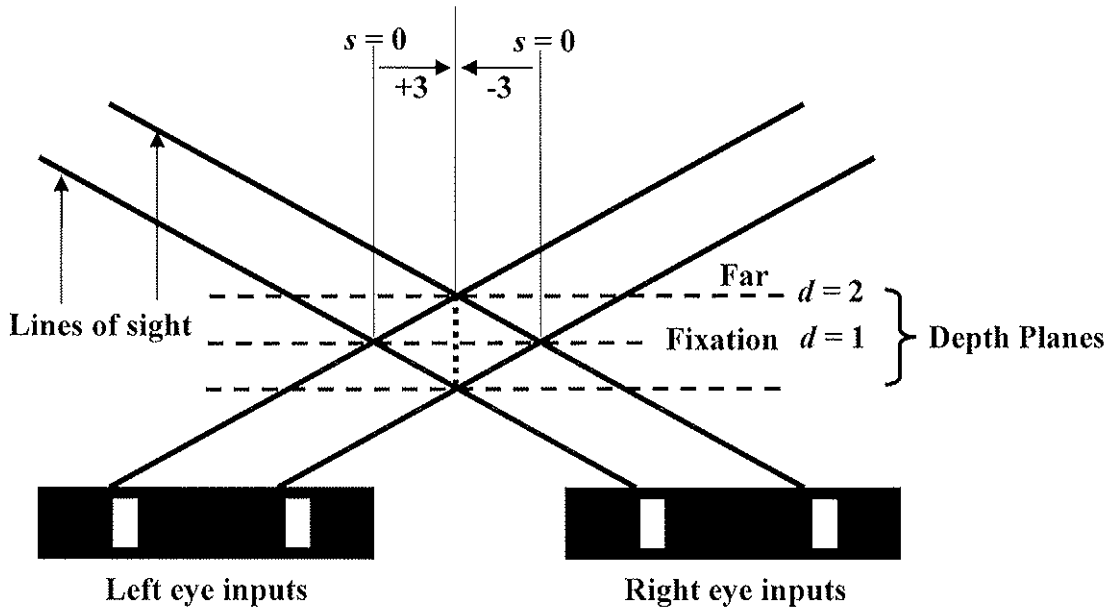

Figure A2

The obligate simple cell activity $b^{(1,B)}_{ijkd}$ is inhibited by all like-oriented inhibitory interneurons at their position (i,j), including those with opposite polarities (indices k and r) via terms $[q^L_{ijkd}]^+ + [q^L_{ijrd}]^+$ and $[q^R_{ijkd}]^+ + [q^R_{ijrd}]^+$ in (13). These eye-specific inhibitory cells at layer 3B with activities $q^{L/R}_{ijkd}$ respond to the vertical orientation (k=1 and 3):

$$\frac{dq^L_{ijkd}}{dt} = -\gamma_2 q^L_{ijkd} + [y^{(1,L)}_{(i+s),jk}]^+ - \beta\left([q^R_{ijkd}]^+ + [q^R_{ijrd}]^+ + [q^L_{ijrd}]^+\right) \tag{14}$$

and

$$\frac{dq^R_{ijkd}}{dt} = -\gamma_2 q^R_{ijkd} + [y^{(1,R)}_{(i-s),jk}]^+ - \beta\left([q^L_{ijkd}]^+ + [q^L_{ijrd}]^+ + [q^R_{ijrd}]^+\right), \tag{15}$$

where γ_2 and β are constants (1 and 5, respectively), and $r = 4 - k$ to provide the opposite-polarity orientation index. As shown in Figure 7, these layer 3B inhibitory cells get excited by layer 4 cells (terms $[y^{(1,L)}_{(i+s),jk}]^+$ and $[y^{(1,R)}_{(i-s),jk}]^+$ on the right hand sides of (14) and (15), respectively) and inhibition from inhibitory interneurons of opposite ocularity with both polarities (reflected by k and r in terms $[q^R_{ijkd}]^+ + [q^R_{ijrd}]^+$ and $[q^L_{ijkd}]^+ + [q^L_{ijrd}]^+$ on the right hand side of (14) and (15), respectively), as well as inhibition from the inhibitory interneuron with opposite polarity with the same ocularity (terms $[q^L_{ijrd}]^+$ and $[q^R_{ijrd}]^+$ on the right hand side of (14) and (15), respectively).

In (13), the same-polarity inhibition (indicated by index k) assures that these binocular simple cells obey an *obligate property* (Poggio, 1991); that is, they can be activated only when they get excitatory input $[y^{(1,R)}_{(i-s),jk}]^+ + [y^{(1,L)}_{(i+s),jk}]^+$ from both ocularities of layer 4 simple cells. The opposite polarity inhibition (indicated by index r) assures that obligate cells do not fuse edges with opposite polarities. A mathematical proof of these properties is described in Grossberg and Howe (2003).

An additional property of the present simulations with regard to the obligate cells is the *size-disparity correlation* (Kulikowski, 1978; Richards and Kaye, 1974; Schor and Tyler, 1981; Schor and Wood, 1983; Schor, Wood, and Ogawa, 1984; Tyler, 1975, 1983). FACADE theory (Grossberg, 1994) exploits the fact that binocularly driven cells with larger receptive fields have a broader range of binocular fusion and can tolerate larger disparity value offsets from their optimum value. This phenomenon implies that many binocular cells can signal the presence of vertical boundaries in more than one depth plane. In the present simulations, we consider two depth planes for simplicity (see Grossberg and Howe (2003) for simulations with more than two depth planes). Obligate cells in both depth planes can hereby signal the vertical edges of 2D images. Obligate cells at both depth planes are assumed to experience a small s (=3) difference in (13) which does not exceed the effective width of their receptive field kernels. This is why, initially and before monocular FIDO feedback, the *vertical* boundaries are present at both depths; see, for example, Figures 11a and 15a.

A5. V1 layer 3B: Monocular simple cells

Figure 7 shows that, besides the vertical binocular simple cells, there are monocular simple cells with activity $b^{(1,L/R)}_{ijk}$ that are driven by monocular simple cells in layer 4 of V1:

$$b^{(1,L/R)}_{ijk} = [y^{(1,L/R)}_{ijk}]^+. \tag{16}$$

A6. V1 layer 2/3: Complex cells

Complex cells of layer 2/3 with activity $z^{(1,L/R/B)}_{ijkd}$ pool opposite polarity input from layer 3B cells. Within a spatial region, complex cells that are tuned to perpendicular orientations also compete. As in layer 3B, layer 2/3 contains both monocular and binocular complex cells, which have their own opposite-polarity pooling and orientational competition independent from each other. The stimulus of Figure 3 and 4 illustrate the importance of such separation, because all contrastive edges there are monocular. Layer 2/3 complex cell activities $z^{(1,L/R/B)}_{ijrd}$ obey:

$$\frac{d}{dt} z_{ijkd}^{(1,L/R/B)} = -z_{ijkd}^{(1,L/R/B)} + (1 - z_{ijkd}^{(1,L/R/B)})([b_{ijkd}^{(1,L/R/B)}]^+ + [b_{ijrd}^{(1,L/R/B)}]^+) - (1 + z_{ijkd}^{(1,L/R/B)}) \sum_{pq} N_{pqij} ([b_{pqKd}^{(1,L/R/B)}]^+ + [b_{pqRd}^{(1,L/R/B)}]^+). \quad (17)$$

In (17), because complex cells pool over opposite polarities, k = 1, 2 (vertical, horizontal). Term $[b_{ijkd}^{(1,L/R/B)}]^+ + [b_{ijrd}^{(1,L/R/B)}]^+$ describes pooling of the like-oriented but opposite-polarity layer 3B inputs with orientation indices k and r, respectively. Indices K and R denote the orientations perpendicular to r and k, respectively with opposite polarity. Term $\sum_{pq} N_{pqij} ([b_{pqKd}^{(1,L/R/B)}]^+ + [b_{pqRd}^{(1,L/R/B)}]^+)$ describes inhibitions from perpendicular orientations (with opposite polarities) within a neighborhood of (i,j) with Gaussian kernel:

$$N_{pqij} = \frac{1}{2\pi\sigma^2} \exp\left(-\frac{1}{2\sigma^2} ((p-i)^2 + (q-j)^2) \right), \quad (18)$$

where $\sigma = 3$ (Figure A1b).

A7. V2 layer 4

Monocular and binocular V1 layer 2/3 cell outputs $z_{ijk}^{(1,L/R)}$ and $z_{ijkd}^{(1,B)}$, respectively, are pooled in layer 4. This hypothesis is consistent with the fact that most cells in V2 are binocular (Hubel and Livingstone, 1987). The activity $y_{ijkd}^{(2)}$ of a V2 layer 4 horizontal cell (k = 2) pools monocular V1 outputs:

$$\frac{d}{dt} y_{ijkd}^{(2)} = -y_{ijkd}^{(2)} + \left[z_{(i+s)jk}^{(1,L)} \right]^+ + \left[z_{(i-s)jk}^{(1,R)} \right]^+ - \delta \sum_{e<d} F(p_{ije}^L + p_{ije}^R). \quad (19)$$

The vertical orientation (k = 1) V2 layer 4 cell pools both monocular and binocular V1 outputs:

$$\frac{d}{dt} y_{ijkd}^{(2)} = -y_{ijkd}^{(2)} + \left[z_{ijkd}^{(1,B)} \right]^+ + \upsilon \left(\left[z_{(i+s)jk}^{(1,L)} \right]^+ + \left[z_{(i-s)jk}^{(1,R)} \right]^+ \right) - \delta \sum_{e<d} (p_{ije}^L + p_{ije}^R). \quad (20)$$

In (19) and (20), parameters υ = 0.20 and δ = 10. The pruning signal $p_{ije}^{L/R}$ of the monocular FIDO (Figure 8, from equation (38)) inhibits $y_{ijkd}^{(2)}$ when the latter is at a farther depth ($e < d$: larger index represent farther depth).

A8. V2 layer 2/3: Bipole grouping cells

The bipole property is realized by interactions between long-range cooperation and short-range competition, as shown in Figure 7. Variable $z_{ijkd}^{(2)}$ represents the bipole cell activity at layer 2/3 of V2:

$$\frac{d}{dt} z_{ijkd}^{(2)} = -z_{ijkd}^{(2)} + (1 - z_{ijkd}^{(2)})([y_{ijkd}^{(2)}]^+ + Q_{ijkd}^{(1)} + Q_{ijkd}^{(2)}) - (z_{ijkd}^{(2)} + \psi)(Q_{ijkd}^{Ix} + Q_{ijkd}^{Io} + Q_{ijkd}^{Id}). \quad (21)$$

The excitatory bottom-up input $[y_{ijkd}^{(2)}]^+$ from layer 4 sums with $Q_{ijkd}^{(1)}$ and $Q_{ijkd}^{(2)}$ which are obtained by convolving elongated half-Gaussian kernels $H_{pqijk}^{(v)}$ with layer 2/3 bipole cell outputs (Figure 7):

$$Q_{ijkd}^{(v)} = \sum_{pq} H_{pqijk}^{(v)} [z_{ijkd}^{(2)} - \rho_z]^+, \quad (22)$$

$v = 1, 2$. Kernels $H^{(1)}_{pqijk}$ and $H^{(2)}_{pqijk}$ in (22) are derived from the Gaussian kernel H_{pqijk} :

$$H_{pqijk} = \frac{1}{2\pi(\sigma_1^2 + \sigma_2^2)} \exp\left(-\frac{1}{2}\left(\frac{(p-i)^2}{\sigma_1^2} + \frac{(q-j)^2}{\sigma_2^2}\right)\right). \tag{23}$$

The horizontally oriented half-Gaussian $H^{(1)}_{pqijk}$ is determined by setting $k = 2$, σ_1 =8, σ_2 =1, and H_{pqijk} to zero when $p < i$. Setting H_{pqijk} to zero when $p > i$ results in $H^{(2)}_{pqijk}$. The vertically oriented half-Gaussian $H^{(1)}_{pqijk}$ is determined by setting $k = 1, \sigma_1 = 1$, σ_2 =8, and H_{pqijk} to zero when $q < j$. Likewise, $q < j$ results in $H^{(2)}_{pqijk}$.

As Figure 7 shows, inhibitory interneurons with activity s_{ijkdv} from both sides (v = 1, 2) inhibit bipole cells in order to realize the selective inward propagation of boundary completion. Correspondingly, the inhibitory terms, Q^{ls}_{ijkd} , in (21) pool the activity of inhibitory interneurons s_{ijkdv} from both sides at each position:

$$Q^{ls}_{ijkd} = \sum_{v=1,2} [s_{ijkdv}]^+ . \tag{24}$$

Inhibitory interneurons with activities s_{ijkdv} get their excitatory input from horizontal connections on the same side of the bipole cell and their inhibitory inputs from the opposite side ($u \neq v$) and the same position (i,j):

$$\frac{d}{dt} s_{ijkdv} = -s_{ijkdv} + Q^{(v)}_{ijkd} - \mu_s s_{ijkdv} [s_{ijkdu}]^+ . \tag{25}$$

Each bipole cell is also inhibited by orientational competition from the bipole cells of the perpendicular orientation ($r \neq k$) within a spatial region around each position (i,j), as implemented by term Q^{lo}_{ijkd} in (21):

$$Q^{lo}_{ijkd} = \sum_{pq}^{r \neq k} N_{pqij} [z^{(2)}_{pqrd} - \rho_z]^+ , \tag{26}$$

where N_{pqij} is the same kernel as in (17).

Vertically oriented bipole cells with activities $z^{(2)}_{ijkd}$ (k = 1) are also influenced by a *disparity filter* that inhibits false binocular matches. Each vertically oriented bipole cell is inhibited by every other vertically oriented bipole cell that shares one of its monocular inputs (Figure A2, oblique line of sight), or is directly in front of or behind it (Figure A2, dashed vertical line): The term Q^{ld}_{ijkd} in (23) provides such inhibition:

$$Q^{ld}_{ijkd} = \omega_1 \sum_{d' \neq d} \left(m_{dd'} \left[z^{(2)}_{(i+s'-s)jkd'} \right]^+ + m_{dd'} \left[z^{(2)}_{(i+s-s')jkd'} \right]^+ + \omega_2 \left[z^{(2)}_{ijkd'} \right]^+ \right). \tag{27}$$

Parameter $m_{dd'}$ = 1.3 when d = 1 (near) and d' = 2 (far). Parameter $m_{dd'}$ = 2.8 when d = 2 (far) and d' = 1 (near). The near plane (fixation plane) is preferred because inhibition from near-to-far is larger than inhibition from far-to-near. As a result, the monocular boundary activities corresponding to the stimulus of Figure 3 will be assigned to zero depth. For the horizontal orientation (k = 2), Q^{ld}_{ijkd} = 0. In the other words, the disparity filter acts on the vertical orientation.

Parameters in (21) - (27) are ψ = 0.9, ρ_z = 0.05 and μ_s = 12 ω_1 = 0.4 and ω_2 = 0.1.

The disparity filter in the 3D LAMINART model of Grossberg and Howe (2003) used a recurrent network equation similar to (27). That model did not, however, include perceptual grouping using bipole cells. Cao and Grossberg (2004) augmented the Grossberg and Howe (2003) model to include bipole-based perceptual grouping, as in the articles of Grossberg and Raizada (2000) and Grossberg and Swaminathan (2004). In addition, Cao and Grossberg (2004), showed how the disparity filter could suppress groupings that correspond to false matches by using an equation like (27). This augmented model was used to explain data about stereopsis and 3D planar surface perception that Grossberg and Howe (2003) could not. The present article shows how this equation can also form part of an explanation of 3D stratification, transparency, and 3D neon color spreading.

A9. Surface representation and monocular FIDO

The monocular Filling-In Domains (FIDOs) respond to the following LGN inputs. The ON FIDO receives the unoriented LGN inputs:

$$X_{ij}^{L/R+} = [\sum_{pq} I_{pq}^{L/R} G_{pqij}]^+, \tag{28}$$

where

$$G_{pqij} = \frac{1}{2\pi\sigma^2} \exp\left(-\frac{1}{2\sigma^2}((p-i)^2 + (q-j)^2)\right) \tag{29}$$

and $\sigma = 4$. The LGN OFF FIDO filling-in inputs are:

$$X_{ij}^{L/R-} = [-\sum_{pq} I_{pq}^{L/R} G_{pqij}]^+. \tag{30}$$

The BCS boundary signals that block filling-in are defined by the sum across all orientations of bipole cell outputs at each position and depth:

$$Z_{ijd} = \sum_{k=1}^{2} z_{ijkd}^{(2)}. \tag{31}$$

Filling-in dynamics are governed by a boundary-gated diffusion equation in which $F_{ijd}^{L/R,+}$ is the monocular Left/Right ON surface signal at position (i, j) and depth d:

$$\frac{d}{dt} F_{ijd}^{L/R+} = -mF_{ijd}^{L/R+} + \sum_{(p,q)\in N_{ij}} (F_{pqd}^{L/R+} - F_{ijd}^{L/R+}) P_{pqijd}^{(M)} + X_{(i\pm s)j}^{L/R+}. \tag{32}$$

The diffusion coefficients, $P_{pqijd}^{(M)}$, in the monocular FIDO are defined by:

$$P_{pqijd}^{(M)} = \frac{\delta}{1 + \varepsilon(Z_{pqd} + Z_{ijd})}, \tag{33}$$

where $\varepsilon = 1{,}000{,}000$, $\delta = 10$, and for $d = 1$ and 2, $s = 0$ and 3, respectively.
LGN inputs are shifted along the line of sight to match their corresponding boundaries at each depth, as reflected by indices $i \pm s$ within $X_{(i\pm s)j}^{L/R+}$ in (32); see Grossberg, Hwang and Mingolla (2002) for how this may happen through learning. At equilibrium, (32) becomes:

$$F_{ijd}^{L/R+} = \frac{X_{(i\pm s)j}^{L/R+} + \sum_{(p,q)\in N_{ij}} F_{pqd}^{L/R+} P_{pqijd}^{M}}{m + \sum_{(p,q)\in N_{ij}} P_{pqijd}^{M}}, \tag{34}$$

where $m = 1$, and the diffusion occurs between nearest neighbors $N_{ij} = \{(i, j-1), (i-1, j), (i+1, j), (i, j+1)\}$. Equation (34) is solved by giving zero initial values to $F_{pqd}^{L/R+}$ and iteratively passing the resultant values of $F_{ijd}^{L/R+}$ to the left hand side of (34) until the recursion equilibrates.

The same dynamics govern OFF filling-in with $F_{ijd}^{L/R-}$ representing the filled-in OFF surface activity:

$$\frac{d}{dt} F_{ijd}^{L/R-} = -mF_{ijd}^{L/R-} + \sum_{(p,q)\in N_{ij}} (F_{pqd}^{L/R-} - F_{ijd}^{L/R-}) P_{pqijd}^{M} + X_{(i\pm s)j}^{L/R-}. \tag{35}$$

At equilibrium, (35) becomes:

$$F_{ijd}^{L/R-} = \frac{X_{(i\pm s)j}^{L/R-} + \sum_{(p,q)\in N_{ij}} F_{pqd}^{L/R-} P_{pqijd}^{M}}{m + \sum_{(p,q)\in N_{ij}} P_{pqijd}^{M}}. \tag{36}$$

The monocular FIDO output is defined by:

$$R_{ijd}^{L/R} = \left[F_{ijd}^{L/R+} - F_{ijd}^{L/R-}\right]^{+}. \tag{37}$$

This double-opponent filled-in signal can cancel when there is a gap in the boundary signal of an edge: The ON filling-in spreads across the gap from one side of it, whereas the OFF filling-in spread across the gap from the other side. Because the ON filling-in activity then equals the OFF filling-in activity on both sides of the boundary gap, they cancel each other in (37). Therefore, any surface whose boundary has a big gap cannot fill-in efficiently unless another connected boundary surrounds it at sufficiently close proximity.

A10. Monocular FIDO output

To generate boundary pruning signals b_{ijd} from the near depth to the far depth in (20) (see Figure 11b), filled-in activities at the Monocular FIDOs are passed through a contrast-sensitive on-center off-surround kernel:

$$\frac{d}{dt} p_{ijd}^{L/R} = -\alpha_b p_{ijd}^{L/R} + (U_b - p_{ijd}^{L/R}) C_{bd}^{L/R} - (L_b + p_{ijd}^{L/R}) E_{bd}^{L/R}. \tag{38}$$

The on-center term

$$C_{bd}^{L/R} = \sum_{(p,q)\in N_{ij}} C_{pq} R_{i+p,j+q,d}^{L/R} \tag{39}$$

has a Gaussian kernel:

$$C_{pq} = \frac{C}{2\pi\sigma_c^2} \exp\left(-\frac{p^2+q^2}{2\sigma_c^2}\right), \tag{40}$$

as does the off-surround term:

$$E_{bd}^{L/R} = \sum_{(p,q)\in N_{ij}} E_{pq} R_{i+p,j+q,d}^{L/R}, \tag{41}$$

where

$$E_{pq} = \frac{S}{2\pi\sigma_s^2} \exp\left(-\frac{p^2 + q^2}{2\sigma_s^2} \right). \quad (42)$$

Parameters in (38)-(42) are α_b=1, U_b=1, L_b=1, C=1, σ_c = 3, S=0.75, σ_s = 3.

A11. Pruned surface signals within the Binocular FIDO

Visible surface signals occur at the binocular FIDOs. Here, binocularly matched LGN signals from both eyes activate depth-selective filling-in domains (pathway 8 in Figure 8), while the contrast-sensitive Monocular FIDO outputs of nearer depths from both eyes prune, or inhibit, redundant surface signals at the same positions and further depths (pathways 9 in Figure 8). The activity ϕ_{ijd} of a Binocular FIDO cell at position (i,j) and depth d thus obeys:

$$\frac{d}{dt}\phi_{ijd}^{+/-} = -\alpha_{bf}\phi_{ijd}^{+/-} + (U_{bf} - \phi_{ijd}^{+/-})(X_{(i+s)j}^{L+/-} + X_{(i-s)j}^{R+/-}) - (L_{bf} + \phi_{ijd}^{+/-}) \sum_{e<d} (p_{ije}^{L} + p_{ije}^{R}), \quad (43)$$

where the LGN inputs are defined by (28) and (30) and the pruning signal by (38). For d = 1 (near), s = 0, and for d = 2 (far), s =3. Parameters U_{bf} and L_{bf} equal 1.

Because there are only two depth planes, the above equation is just applicable when d = 2 and e = 1, equivalent to the pruning of the far depth by the near depth (larger depth index means farther).

A12. Binocular FIDO surface formation using enriched boundaries

Finally, activities $\mu_{ijd}^{+/-}$ represent the ON and OFF filled-in surface representation at the Binocular FIDOs:

$$\frac{d}{dt}\mu_{ijd}^{+/-} = -m\mu_{ijd}^{+/-} + \sum_{(p,q)\in N_{ij}} (\mu_{pqd}^{+/-} - \mu_{ijd}^{+/-}) P_{pqijd}^{B} + \phi_{ijd}^{+/-}. \quad (44)$$

In (44), terms P_{pqijd}^{B} represent the boundary-gated permeabilities:

$$P_{pqijd}^{B} = \frac{\delta}{1 + \varepsilon(\xi_{pqd} + \xi_{ijd})}. \quad (45)$$

At the binocular FIDOs, the boundaries that determine gating are enriched (e.g., Figure 15c and 18b) by adding all nearer boundaries at each position:

$$\xi_{ijd} = \sum_{e \le d} Z_{ije}. \quad (46)$$

The same method used to solve (34) is used for (44). The double-opponent filled-in activity, $R_{ijd}^{(B)}$, represents the visible surface percept:

$$R_{ijd}^{(B)} = \left[\mu_{ijd}^{+} - \mu_{ijd}^{-} \right]^{+}. \quad (46)$$

References

Adelson, E.H. (2000). Lightness Perception and Lightness Illusions. In: M. Gazzaniga (Ed.), *The New Cognitive Neurosciences* (pp. 339-351). 2nd Ed. Cambridge, MA: MIT Press.

Anderson, BL. (1997). A theory of illusory lightness and transparency in monocular and binocular images: the role of contour junctions. *Perception*, *26*:419-53

Cao, Y., & Grossberg S. (2004). A laminar cortical model of stereopsis and 3D surface perception: Closure and da Vinci stereopsis. Submitted for publication

DeWeerd, P., Peralta, M.R., Desimone, R., & Ungerledier, L.G. (1999). Loss of attentional stimulus selection after extrastriate cortical lesions in macaques. *Nature Neuroscience*, *2*, 753-758

Grossberg S. (1980). How does a brain build a cognitive code? *Psychological Review, 87*:1-51

Grossberg S. (1994). 3-D vision and Figure-ground separation by visual cortex. *Perception and Psychophysics*, *55*: 48-121

Grossberg S. (1997). Cortical dynamics of three-dimensional Figure-ground perception of two-dimensional pictures, *Psychological Review, 104*:618-58

Grossberg S. (1999a). How does the cerebral cortex work? Learning, attention, and grouping by the laminar circuits of visual cortex. *Spatial Vision, 12*:163-85

Grossberg S. (1999b). The link between brain learning, attention, and consciousness. *Consciousness and Cognition*, *8*:1-44

Grossberg S. (2003). Filling-in the forms: Surface and boundary interactions in visual cortex. In L. Pessoa, & P. DeWeerd (Eds.), *Filling-In: From Perceptual Completion to Cortical Reorganization* (pp.13-37). New York: Oxford University Press.

Grossberg, S., & Howe, P.D.L. (2003). A laminar cortical model of stereopsis and three-dimensional surface perception. *Vision Research*, *43*:801-29

Grossberg S, Hwang S, Mingolla E. (2002). Thalamocortical dynamics of the McCollough effect: boundary-surface alignment through perceptual learning. *Vision Research*, *42*:1259-86

Grossberg S, & Mingolla E. (1985a). Neural dynamics of perceptual grouping: textures, boundaries, and emergent segmentations. *Perception and Psychophysics*, *38*:141-71

Grossberg S, & Mingolla E. (1985b). Neural dynamics of form perception: boundary completion, illusory figures, and neon color spreading. *Psychological Review*, *92*:173-211

Grossberg S, Mingolla E, & Ross WD. (1997). Visual brain and visual perception: how does the cortex do perceptual grouping? *Trends in Neurosciences*, *20*:106-11

Grossberg S, & Raizada RD. (2000). Contrast-sensitive perceptual grouping and object-based attention in the laminar circuits of primary visual cortex, *Vision Research*, *40*:1413-32

Grossberg S, & Seitz A. (2003). Laminar development of receptive fields, maps and columns in visual cortex: the coordinating role of the subplate, *Cerebral Cortex*, *13*:852-63

Grossberg S. & Swaminathan G. (2003). A laminar cortical model for 3D perception of slanted and curved surfaces and of 2D images: Development, attention, and bistability Technical Report CAS/CNS TR-2003-002, Boston University. Submitted for publication

Grossberg S, & Todorovic D. (1988). Neural dynamics of 1-D and 2-D brightness perception: a unified model of classical and recent phenomena, *Perception and Psychophysics*, *43*: 241-77

Grossberg S., & Yazdanbakhsh A. (2003a). Laminar cortical dynamics of 3D surface stratification, transparency, and neon spreading. *3rd annual meeting of Vision Sciences Society, FR43,* pp. 77

Grossberg S., & Yazdanbakhsh A. (2003b). Laminar Cortical Mechanisms of 3D Surface Processing, *Society for Neuroscience 33rd annual meeting*, 339.5

Hubel, D. H., & Livingstone, M. S. (1987). Segregation of form, color, and stereopsis in primate area 18. *The Journal of Neuroscience*, *7,* 3378-3415.

Hubel DH, & Wiesel TN. (1968). Receptive fields and functional architecture of monkey striate cortex, *Journal of Physiology*, *195*:215-43

Kelly F, & Grossberg S. (2000). Neural dynamics of 3-D surface perception: Figure-ground separation and lightness perception, *Perception and Psychophysics*, *62*:1596-618

Kulikowski JJ. (1978). Limit of single vision in stereopsis depends on contour sharpness, *Nature. 275*: 126-7

Metelli F. (1974). The perception of transparency, *Scientific American*, *230*:90-8

McGuire BA, Hornung JP, Gilbert CD, & Wiesel TN. (1984). Patterns of synaptic input to layer 4 of cat striate cortex. *Journal of Neuroscience*, *4*:3021-33

Nakayama K. (1996). Binocular visual surface perception *Proceedings of the National Academy of Sciences U S A, 23;93*:634-9

Poggio, G. F. (1991). Physiological basis of stereoscopic vision. In *Vision and Visual Dysfunction. Binocular vision* (pp. 224-238). Boston, MA: CRC

Polat U, & Sagi D. (1993). Lateral interactions between spatial channels: suppression and facilitation revealed by lateral masking experiments, *Vision Research*, 33(7):993-9

Raizada RD, & Grossberg S. (2003). Towards a theory of the laminar architecture of cerebral cortex: computational clues from the visual system, *Cerebral Cortex*, *13*:100-13

Richards W, & Kaye MG. (1974). Local versus global stereopsis: two mechanisms? *Vision Research.14*: 1345-7

Schor CM, & Tyler CW. (1981). Spatio-temporal properties of Panum's fusional area, *Vision Research, 21*: 683-92

Schor CM, & Wood I. (1983). Disparity range for local stereopsis as a function of luminance spatial frequency, *Vision Research, 23*: 1649-54

Schor C, Wood I, & Ogawa J. (1984). Binocular sensory fusion is limited by spatial resolution. *Vision Research, 24*:661-5

Takeichi H, Shimojo S, & Watanabe T. (1992). Neon flank and illusory contour: interaction between the two processes leads to color filling-in. *Perception*, *21*:313-24

Tucker TR, & Katz LC. (2003a). Recruitment of local inhibitory networks by horizontal connections in layer 2/3 of ferret visual cortex. *Journal of Neurophysiology, 89*:501-12

Tucker TR, Katz LC. (2003b). Spatiotemporal patterns of excitation and inhibition evoked by the horizontal network in layer 2/3 of ferret visual cortex. *Journal of Neurophysiology*, *89*:488-500

Tyler CW. (1975). Spatial organization of binocular disparity sensitivity, *Vision Research, 15*: 583-90

Tyler CW. (1983). Sensory processing of binocular disparity. In C. M. Schor & K. J. Cuiffreda (Eds.), *Vergence eye movements* (pp. 199-295). Boston: Butterworths

von der Heydt R, Peterhans E, Baumgartner G. (1984). Illusory contours and cortical neuron responses, *Science*, *224*:1260-2

Watanabe T, Cavanagh P. (1993). Surface decomposition accompanying the perception of transparency, *Spatial Vision,* 7:95-111

Watanabe T, Cavanagh P. (1993). Transparent surfaces defined by implicit X junctions, *Vision Research*, *33*:2339-46